CaV1 and CaV2 calcium channels mediate the release of distinct pools of synaptic vesicles

Brian D. Mueller[1#], Sean A. Merrill[1#], Shigeki Watanabe[1], Ping Liu[2], Anish Singh[1], Pablo Maldonado-Catala[3], Alex Cherry[1], Malan Silva[1], Andres Villu Maricq[3], Zhao-Wen Wang[2], Erik M. Jorgensen[1*]

[1] Howard Hughes Medical Institute, School of Biological Sciences, University of Utah, Salt Lake City, UT

[2] Department of Neuroscience, University of Connecticut Medical School, Farmington, CT

[3] Department of Neurobiology, University of Utah, Salt Lake City, UT

* Lead contact

[#] Authors contributed equally towards this work

Abstract

Activation of voltage-gated calcium channels at synapses leads to local increases in calcium and the fusion of synaptic vesicles. However, presynaptic output will be determined by the density of calcium channels, the dynamic properties of the channel, the distance to docked vesicles, and the release probability at the docking site. We demonstrate that at *C. elegans* neuromuscular junctions two different classes of voltage-gated calcium channels, CaV2 and CaV1, mediate the release of distinct pools of synaptic vesicles. CaV2 channels are concentrated in densely packed clusters ~300 nm in diameter with the active zone proteins Neurexin, α-Liprin, SYDE, ELKS/CAST, RIM-BP, α-Catulin, and MAGI1. CaV2 channels mediate the fusion of vesicles docked adjacent to the dense projection and are colocalized with the synaptic vesicle priming protein UNC-13L. By contrast, CaV1 channels are dispersed in the synaptic varicosity and are coupled to internal calcium stores via the ryanodine receptor. CaV1 and ryanodine receptor mediate the fusion of vesicles docked broadly in the synaptic varicosity and are colocalized with the vesicle priming protein UNC-13S. Distinct synaptic vesicle pools, released by different calcium channels, could be used to tune the speed, voltage-dependence, and quantal content of neurotransmitter release.

Keywords: L-type, N-type calcium channels, super-resolution microscopy, Munc13-1, bMunc13-2, Ryanodine receptor. NRX-1, SYD-2, SYD-1, ELKS-1, RIMB-1, CTN-1, MAGI-1.

Introduction

Synaptic vesicles fuse to the plasma membrane within the presynaptic bouton in a domain called the active zone, and the intricate molecular architecture within the active zone determines the dynamics of the neurotransmitter release (Guzikowski & Kavalali, 2021). Vesicle fusion is driven by calcium influx and binding to the calcium sensor synaptotagmin on the synaptic vesicle (Geppert et al., 1994; Littleton, Stern, Schulze, Perin, & Bellen, 1993; Ward, Weber, & Chapman, 2004). The coupling of fusion sites to calcium channels determines the transfer function of synapses to depolarizing inputs (Eggermann, Bucurenciu, Goswami, & Jonas, 2012; Eguchi, Montanaro, le Monnier, & Shigemoto, 2022; Özçete & Moser, 2021; Rebola et al., 2019), and thus synaptic activity depends on three features of calcium influx: the dynamic properties of the calcium channel, the concentration of calcium at the fusion site, and the release probability of the vesicle. These features are dictated by calcium channel type and location, by the distance to docked vesicles, and by the activity of the priming protein Unc13. Here, we characterize these features at the *C. elegans* neuromuscular junction.

50 Voltage-gated calcium channels can be divided into three molecular families: CaV1,
51 CaV2, and CaV3, each with fundamentally different dynamic properties, including voltage-
52 sensitive activation and inactivation (Catterall, Perez-Reyes, Snutch, & Striessnig, 2005;
53 Nowycky, Fox, & Tsien, 1985). Each of these channel classes is primarily associated with
54 tissue-specific functions: In muscle, CaV1 (L-type) channels mediate contraction and are
55 coupled to the ryanodine receptor to release internal calcium stores (RyR). In neurons, CaV2
56 (P/Q, N, and R-type) channels drive synaptic transmission. In neurons and excitable cells, CaV3
57 (T-type) regulate action potential oscillations and pacemaker frequencies (Dolphin, 2021) These
58 tissue-specific roles are not exclusive, for example, the CaV1 variants CaV1.3 and CaV1.4 are
59 associated with neurotransmitter release in hair cells and photoreceptors, respectively (Dolphin
60 & Lee, 2020).
61
62 In the nematode *C. elegans*, each class is encoded by a single gene: CaV1 (*egl-19*),
63 CaV2 (*unc-2*), CaV3 (*cca-1*), and RyR (*unc-68*). In all animals, CaV2 is the main calcium
64 channel for synaptic transmission (Richmond, Weimer, & Jorgensen, 2001; Smith et al., 1996;
65 Tsien, Lipscombe, Madison, Bley, & Fox, 1988; Tsien & Tsien, 1990; Zheng et al., 1995). Unlike
66 other animals, nematodes lack voltage-gated sodium channels and neurotransmission is
67 mediated via graded release (Liu, Chen, & Wang, 2014; Liu, Hollopeter, & Jorgensen, 2009). In
68 *unc-2* mutants, which lack the CaV2 channel, the frequency of tonic miniature currents ('minis')
69 is severely reduced, but some release remains (Richmond et al., 2001; Tong et al., 2017).
70 Physiological studies suggest CaV1 can also contribute to neurotransmission; CaV1 channel
71 blockers reduce tonic minis (Tong et al., 2017). However, the role of CaV1 channels at
72 synapses in *C. elegans* is complicated because CaV1 also contributes to calcium-mediated
73 action potentials in neurons and is required in the body muscle for viability (Lee, Lobel,
74 Hengartner, Horvitz, & Avery, 1997; Liu, Kidd, Dobosiewicz, & Bargmann, 2018). Finally, the
75 ryanodine receptor also contributes to neurotransmission, and is specifically required for
76 multivesicular release (Chen et al., 2017; Liu et al., 2005).
77
78 After the channels close, the concentration of calcium at the site of vesicle fusion will
79 rapidly decline by diffusion (Dittman & Ryan, 2019). Free calcium will be further depleted by
80 calcium buffers and calcium pumps (Blaustein, 1988; Eggermann et al., 2012). Because
81 intracellular calcium is extremely low (0.05 μM), and levels required for fusion are relatively high
82 (half-maximal 10 μM) (Courtney, Briguglio, Bradberry, Greer, & Chapman, 2018;
83 Schneggenburger & Neher, 2000), the effective range of calcium around a single voltage-gated
84 calcium channel is modeled to be only 20 nm for evoked fusion, a 'nanodomain' not much larger
85 than the diameter of the calcium channel itself (Fedchyshyn & Wang, 2005; Weber et al., 2010).

86 For synapses to reliably track high frequency action potentials, there must be a large number of
87 channels to negate the stochastic nature of channel opening, and the channels must be tightly
88 coupled to the release sites in this nanodomain. Thus, the transfer function not only depends on
89 the identity of the calcium channel, but also depends on the density of calcium channels and the
90 distance to the docked vesicle. Nevertheless, some synapses rely on 'loose' coupling to calcium
91 channels. Calcium microdomains - larger than 100 nm - can drive synaptic vesicle fusion,
92 suggesting that some calcium signals are more robust and do not require tight physical coupling
93 (Eggermann et al., 2012; Vyleta & Jonas, 2014). The tuning of the output of the presynapse
94 then ultimately depends on the spatial and temporal organization of the calcium signal at the
95 release site (Eggermann et al., 2012; Nakamura et al., 2015).
96
97 The presence of docked vesicles at release sites and the probability of vesicle fusion
98 depends on the active zone protein Unc13 (Dittman, 2019; Neher & Brose, 2018). Unc13
99 tethers vesicles to the active zone membrane through C2B and C2C domains which flank the
100 MUN domain (Imig et al., 2014; Quade et al., 2019). The central MUN domain interacts with the
101 SNARE protein syntaxin (Augustin, Rosenmund, Südhof, & Brose, 1999; Lai et al., 2017; Yang
102 et al., 2015) and promotes the open state of syntaxin to initiate SNARE pairing (Richmond et al.,
103 2001). Alternative structural isoforms of Unc13 are distinguished by the presence or absence of
104 a C2A domain at the N-terminus (UNC-13-Long and UNC-13-Short, respectively in *C. elegans*)
105 (Dittman, 2019). Binding of the C2A domain to the scaffolding protein RIM activates these
106 Unc13 isoforms (Betz et al., 2001; Hu, Tong, & Kaplan, 2013; Liu et al., 2019; Lu et al., 2006;
107 Zhou, Stawicki, Goncharov, & Jin, 2013). Unc13 isoforms, which lack a C2A domain, have been
108 demonstrated to bind ELKS / CAST in flies and mice (Böhme et al., 2016; Kawabe et al., 2017).
109 In the absence of Unc13, synaptic vesicles fail to dock at release sites (Hammarlund,
110 Palfreyman, Watanabe, Olsen, & Jorgensen, 2007; Imig et al., 2014; Richmond, Davis, &
111 Jorgensen, 1999; Siksou et al., 2009). Moreover, binding of DAG and calcium to Unc13
112 regulates the differential release probabilities of primed vesicles (Basu, Betz, Brose, &
113 Rosenmund, 2007; Michelassi, Liu, Hu, & Dittman, 2017; Neher & Brose, 2018).
114
115 Here, we demonstrate in *C. elegans* that two different classes of voltage-gated calcium
116 channels, CaV2 (UNC-2) and CaV1 (EGL-19) mediate the release of two physiologically distinct
117 pools of synaptic vesicles. A third calcium channel, the ryanodine receptor (RyR / UNC-68), is
118 essential for CaV1-mediated vesicle release. Time-resolved electron microscopy in mutants
119 demonstrates that these channels mediate fusion of spatially distinct pools of synaptic vesicles
120 in the same synaptic varicosity. Finally, we use super-resolution fluorescence microscopy to
121 demonstrate that CaV2 is localized with UNC-13L at the dense projection, and that CaV1 and

122 RyR colocalize with UNC-13S at distal sites. Altogether, we describe two pools of synaptic
123 vesicles: (1) The central pool is localized adjacent to the dense projection, vesicles are docked
124 by UNC-13L, and released by a dense cluster of CaV2 channels. (2) The lateral pool of vesicles
125 is broadly distributed, docked by UNC-13S, and released by dispersed CaV1 and RyR
126 channels.
127
128 **Results**
129 **CaV1 and CaV2 calcium channels are required semi-redundantly for nervous system**
130 **function**
131 The genome of *C. elegans* contains only a single gene for each major voltage-gated
132 calcium channel class: CaV1 (*egl-19*), CaV2 (*unc-2*), CaV3 (*cca-1*), and a single calcium-gated
133 RyR (*unc-68*) (hereafter, referred to by their common names). Loss of the CaV3 T-type channel
134 does not affect neurotransmitter release in acetylcholine neurons (Liu et al., 2018). However,
135 loss of any other calcium channel results in impaired neurotransmission (Liu et al., 2005;
136 Richmond et al., 2001; Tong et al., 2017). Null mutants lacking either CaV2 (*unc-2*(*lj1)*) or RyR
137 (*unc-68*(*e540*)) are viable, but CaV1 null mutants (*egl-19*(*st556)*) die as embryos due to a loss
138 of muscle function during morphogenesis (Lee et al., 1997). We rescued the CaV1 null mutant
139 using a muscle promoter expressed early in development; since this strain lacks CaV1 in the
140 nervous system, we refer to it as 'CaV1(Δns)'.
141
142 To determine whether these channels function cooperatively or in parallel, we tested for
143 synthetic interactions between mutations of these channel types. The double mutant CaV1(Δns)
144 RyR is viable, and is no worse than the RyR null, consistent with their coupled function (Figure
145 1A). However, CaV1(Δns) CaV2(-) double mutants and RyR(-) CaV2(-) double mutants exhibit a
146 synthetic lethal interaction. These data suggest that calcium influx from CaV1-RyR acts
147 redundantly, and in parallel, with CaV2 to sustain neurotransmission.
148
149 CaV1(Δns) animals are uncoordinated, and the phenotypes are fully rescued by the
150 expression of CaV1 in the nervous system (Figure 1B). To determine the role of CaV1 on
151 locomotion, we characterized crawling using worm tracker software. CaV1(Δns) worms travel
152 shorter distances than wild-type worms, consistent with slower crawling speeds (Figure 1C,D).
153 In addition, wild-type animals spent longer time and travelled longer distances during forward
154 bouts (Figure 1E,F). Conversely, CaV1(Δns) worms traveled shorter distances and initiated
155 reversals more frequently than the wild type (Figure 1G). However, the distance travelled while
156 backing tended to be shorter in the CaV1(Δns) animals; whereas the rescued animals travelled
157 longer distances in reverse, about a full body length (Figure 1H). Reversals in all three

158 genotypes were similar in duration (Figure 1I). These results indicate that CaV1 functions in the
159 nervous system for speed of locomotion, and also biases the bistable locomotory circuit toward
160 forward locomotion (Zheng, Brockie, Mellem, Madsen, & Maricq, 1999).
161
162 **CaV2 and CaV1 regulate distinct pools of synaptic vesicles**
163 To determine if CaV1 is playing a direct role in synaptic transmission, as well as the
164 depolarization state of the locomotory circuit, we recorded synaptic currents at neuromuscular
165 junctions. Body muscles were voltage-clamped at a holding potential of -60mV, and miniature
166 postsynaptic currents recorded. Miniature postsynaptic currents ('minis') are caused by the
167 release of neurotransmitter from one or a few synaptic vesicles. The nematode neuromuscular
168 junction releases neurotransmitter via graded release (Liu et al., 2014; Liu et al., 2009); the
169 frequency of tonic minis drive calcium action potentials in the muscles (Liu et al., 2011).
170
171 The rate of miniature postsynaptic currents (minis/s) compared to the wild type (32.2 +/-
172 2.1 minis/s) is significantly reduced in each of the single mutants, CaV2 (18.7 +/- 3.5 minis/s),
173 CaV1(Δns) (18.7 +/- 3.6 minis/s), and RyR (20.9 +/- 1.5 minis/s) (Figure 2A). Because some of
174 the channel double mutants are synthetic lethal, we acutely blocked CaV1 using nemadipine
175 (Kwok et al., 2006). The frequency of minis in the wild-type with nemadipine (+nema 18.4 +/- 2
176 minis/s) was similar to CaV1(Δns) and did not further reduce mini frequency in the CaV1(Δns)
177 mutant (+nema 19.1 +/- 2.7 mini/s), demonstrating that nemadipine is an effective blocker of
178 CaV1 and does not block CaV2 nonspecifically. Nemadipine application on the RyR mutant did
179 not exacerbate the phenotype ('RyR(-) +nema', 20.7 +/- 1.3 mini/s), indicating that RyR and
180 CaV1 function interdependently at neuromuscular junctions. To determine if CaV1 and CaV2
181 are required together for all neurotransmitter release, we blocked CaV1 in the CaV2 mutant.
182 Application of nemadipine almost completely abolished mini frequency in the CaV2 mutant
183 (+nema 1.7 +/- 0.6 mini/s). We conclude that all vesicle fusion at neuromuscular junctions relies
184 on CaV1 and CaV2, each contributing about half of the minis. In addition, calcium influx through
185 CaV1 is not sufficient for vesicle fusion; CaV1 relies on internal calcium stores released by RyR
186 to fuse synaptic vesicles.
187
188 We confirmed these conclusions by making viable double mutants. Similar to the
189 nemadipine experiments, the rate of minis in the CaV1(Δns) RyR double mutant (19.6 +/- 2
190 mini/s) is similar to the single CaV1(Δns) and RyR mutants, again suggesting that CaV1 relies
191 on coupling to RyR to activate neurotransmitter release. To generate strains that bypass the
192 synthetic lethality with CaV2, we expressed CaV2 in head neurons using a tissue-specific
193 promoter ('P*unc-17*h') (Hammarlund et al., 2007; Topalidou et al., 2016). Expression of CaV2 in

194 the head neurons of CaV2 nulls, referred to as 'CaV2(Δnmj)', bypassed the synthetic lethality of
195 both the CaV1(Δns) CaV2(-) double mutant, and the RyR(-) CaV2(-) double mutant, but the
196 rescued animals exhibit a synthetic paralyzed phenotype. The mini rates of CaV2(Δnmj)
197 CaV1(Δns) double mutants (12.8 +/- 2.4 mini/s) and CaV2(Δnmj) RyR double mutants (11.3 +/-
198 2.1 mini/s) are significantly diminished, but not completely abolished (Extended Data Figure 2A).
199 The lingering neuronal activity in these strains is likely due to CaV2 expression from head-
200 rescued CaV2 neurons synapsing onto the muscles (the sublateral cord motor neurons).
201 Nevertheless, they demonstrate that CaV1 and RyR are in the same pathway, and act in
202 parallel to CaV2.
203
204 **RyR is required for multiquantal release**
205 The mode of mini amplitudes represents miniature currents from single vesicle fusions,
206 and the modal value is similar in all strains (WT 10 pA, CaV1Δns 10pA, RyR 11pA, CaV2 8pA)
207 regardless of nemadipine treatment (N2+nema 10pA, CaV1Δns+nema 8pA, RyR+nema 10pA,
208 CaV2+nema 11pA) (Figure 2E, Extended Data Figure 2D). However, the mean amplitude of
209 miniature currents is reduced in the RyR(-) mutant (15.5 ±0.6 pA) compared to the wild type
210 (22.3 ±1.9 pA; Figure 2B-D, Extended Data Figure 2B,E). The reduction in mini amplitudes is
211 likely due to a loss of multiquantal release since the focus of ryanodine receptor function is in
212 neurons (Chen et al., 2017; Liu et al., 2005).
213
214 CaV2 is also functionally coupled to RyR to drive multiquantal release. Mini amplitudes
215 from CaV2 and RyR can be observed when CaV1 channels are blocked by nemadipine
216 (22.6 ±2.1 pA, 'wild-type + nemadipine', Fig. 2E). Mini amplitudes solely from CaV2 are
217 reduced in the absence of RyR (14 +/- 0.9pA, 'RyR + nemadipine'), suggesting that RyR also
218 responds to calcium from CaV2. Further, fitting the frequency distribution of mini amplitudes to
219 multiple gaussians indicate that most multiquantal events are driven by RyR (Figure 2F), though
220 some multiquantal events may be attributed to CaV2 (Figure 2G).
221
222 Together, these data demonstrate that CaV2 and CaV1 channels regulate the release of
223 separate synaptic vesicle pools at neuromuscular junctions. CaV1 requires the ryanodine
224 receptor for vesicle fusion. Calcium influx through CaV2 is sufficient to fuse vesicles although
225 neurotransmitter release is amplified by the ryanodine receptor.
226
227 **CaV2 and CaV1 mediate fusion of separate vesicle pools at single synapses**
228 The physiology data suggest that CaV2 and CaV1 mediate the release of distinct
229 synaptic vesicle pools onto muscles. To demonstrate these calcium channels regulate spatially

230 distinct pools at the same synaptic varicosity, time-resolved “flash-and-freeze” electron
231 microscopy was used to characterize fusing vesicle pools (Watanabe et al., 2013). Transgenic
232 animals expressing channelrhodopsin in acetylcholine neurons were loaded into a high-
233 pressure freezing chamber, and stimulated with a 20-ms light pulse to depolarize neurons and
234 activate synaptic calcium channels. Animals were frozen 50 ms after stimulation; control
235 animals were treated identically but not stimulated. Frozen samples were fixed by freeze
236 substitution, embedded in plastic and sectioned for electron microscopy (Watanabe et al.,
237 2013). Docked vesicles are defined as those in contact with the plasma membrane; docking
238 was segmented blind to treatment and genotype (Figure 3A,B). The distance from the dense
239 projection to the docked vesicle is plotted on the X-axis (Figure 3C). Decreases in docked
240 vesicles after stimulation are assumed to be the result of synaptic vesicle fusion, although
241 calcium influx could cause some vesicles to undock and return to the cytoplasm (Kusick et al.,
242 2020).
243
244 To identify vesicle fusions associated with particular calcium channels, we analyzed the
245 distribution of docked vesicles in mutant animals. In unstimulated animals, docked vesicles are
246 clustered around dense projections, although many are observed at lateral regions extending
247 hundreds of nanometers from dense projections. Docked vesicles are uniformly depleted after
248 stimulation in wild-type animals (Figure 3D). Genetic ablation of CaV2 channels reduced vesicle
249 fusions adjacent to the dense projection; docked vesicles distal to the dense projection still
250 fused in response to stimulation (Figure 3E). To assay CaV1 function, we analyzed the
251 hypomorph *egl-19(n582)* to avoid the lethality observed in the double mutants. Mutation of the
252 CaV1 channel reduced fusion broadly, although significant vesicle fusions were observed within
253 100 nm of the dense projection (Figure 3F). In the absence of RyR only CaV2 is functional, and
254 vesicle fusions are only observed in the 33 nm pool —directly adjacent to the dense projection
255 (Figure 3G). The CaV1 CaV2 double mutant exhibited no change in the number and distribution
256 of docked synaptic vesicles after stimulation (Figure 3H). Together, these data demonstrate that
257 *C. elegans* neuromuscular junctions have two spatially distinct pools of synaptic vesicles: a
258 central pool dependent on CaV2 calcium channels and a lateral pool dependent on CaV1 and
259 RyR.
260
261 **CaV2 and CaV1 differentially localized at synapses**
262 The electron microscopy data suggest that CaV1 and CaV2 are localized to spatially
263 separate areas of the active zone. To localize calcium channels with normal expression levels,
264 we tagged the endogenous genes and localized the proteins using fluorescence microscopy.
265 We performed 3-color imaging using dense projection markers as an anatomical fiducial at the

266 center of the synapse. Because *C. elegans* synaptic varicosities are less than 1μm in diameter,
267 super-resolution microscopy was required to resolve channel clusters. A segment of the dorsal
268 nerve cord was imaged, and the region of imaging was restricted to a narrow band to avoid
269 potential complications by CaV1 expression in muscle. To ensure that the pattern of synapses
270 in our fluorescence images matched the arrangement of neuromuscular junctions, we
271 reconstructed 20 μm of the dorsal cord. All imaging was conducted on living, acutely
272 anesthetized nematodes.
273
274 Multiple tagging sites were tested for all genes, but in some cases the tags disrupted
275 function or the splice isoforms were not expressed in neurons. Therefore, we tagged internal
276 sites within regions of poor conservation (Extended Data Figure 4A,B). For example, CaV2 was
277 tagged with HALO (Los et al., 2008) in the second extracellular loop near the N-terminus
278 (Kurshan et al., 2018; Schwartz & Jorgensen, 2016).
279
280 To confirm that the pattern of calcium channels in our fluorescence images matched the
281 arrangement of dense projections, we reconstructed 20 μm of the dorsal nerve cord from serial
282 sections for electron microscopy (Figure 4A). CaV2 / UNC-2 channels have been localized to
283 the dense projection by immuno-electron microscopy in the nematode (Gracheva, Hadwiger,
284 Nonet, & Richmond, 2008). CaV2 clusters are localized every 1.10 +/- 0.16 μm along the dorsal
285 cord by super-resolution microscopy, similar to the distribution of dense projections in the
286 reconstruction (1.02 / μm). To identify proteins associated with CaV2, we tagged multiple active
287 zone components implicated in scaffolding and release complexes at the dense projection
288 (Ackermann, Waites, & Garner, 2015; Südhof, 2012). Neurexin (*nrx-1*), Magi (*magi-1*), Syde1
289 (*syd-1*), Liprin-α (*syd-2*), RIMBP (*rimb-1*), and α-Catulin (*ctn-1*) were tagged with SkylanS. Each
290 of these proteins is closely associated with CaV2::HALO puncta placing them at the dense
291 projection as well (Figure 4B).
292
293 ELKS clusters in particular are tightly associated with CaV2 clusters (Figure 4C), and will
294 serve as a synaptic fiducial for CaV2 and CaV1 comparisons. To quantify the distribution of
295 CaV2 relative to ELKS, an axis was plotted between the two cluster centers, and localizations
296 collapsed onto this axis. CaV2 localizations along the axis to the ELKS cluster center were
297 measured and plotted as a histogram (Figure 4D). CaV2 clusters and ELKS clusters are similar
298 in diameter (297 nm vs 294 nm, respectively). However, only 62% of ELKS localizations are
299 within a CaV2 cluster (Figure 5A-C); the cluster centers are slightly offset (124nm). The offset
300 may be because the proteins domains overlap but are not coincident, or alternatively, these
301 proteins may be perfectly colocalized but differ in our plot due to the positions of the tags on the

302 proteins; specifically, CaV2 is tagged on the extracellular side, whereas ELKS is tagged at the
303 C-terminus on the intracellular side. In contrast to the highly concentrated subsynaptic
304 distribution of CaV2, CaV1 is broadly distributed as dispersed puncta (diameter 869 nm), mostly
305 separate from ELKS (262 nm from ELKS center to CaV1 center of mass) (Figure 5A,B), and
306 shares only a 24% overlap with ELKS or CaV2. CaV1 is largely excluded from CaV2 clusters,
307 but the clusters often abut one another (Figure 5C).
308
309 To confirm that the CaV1 localizations are presynaptic and not in the muscle or
310 epidermis, we generated a HALO-tagged CaV1 under the pan-neuronal synaptotagmin
311 promotor (P*snt-1*). This construct was inserted in the CaV1(Δns) strain, and fully rescued CaV1
312 function (Figure 1B-I). For convenience of genetic crosses, we used RIM binding-protein
313 (RIMBP/RIMB-1) as the dense projection marker. The overexpressed CaV1::HALO tends to be
314 more punctate than the endogenously tagged protein (Extended Data Figure 5A,B). However,
315 CaV1 is not colocalized with RIMBP and the distances between clusters are similar to the
316 endogenously tagged gene (center-to-center CaV1, endogenous tag to ELKS: 262nm;
317 transgene tag to RIMBP: 378 nm)(Extended Data Figure 5C). To demonstrate that CaV1
318 clusters are presynaptic, we assayed colocalization with a presynaptic marker. LIN7 / VELI is a
319 potential CaV1 scaffolding protein via PDZ domain interactions (Butz, Okamoto, & Südhof,
320 1998; Pym et al., 2017). We expressed LIN7 in acetylcholine motor neurons using the *unc-129*
321 promotor (Extended Data 5D). CaV1 and LIN7 clusters are closely associated, but not
322 associated with RIMBP (Extended Data Figure 5E). These data suggest that CaV1 is localized
323 at presynaptic boutons in a separate domain from CaV2 channels.
324
325 If CaV1 and RyR function in the same vesicle fusion pathway, they should be
326 colocalized (Piggott & Jin, 2021). RyR was tagged with HALO at the N-terminus of the neuronal
327 isoform (Extended Data Figure 4C) (Marques et al., 2020). RyR localizations were compared to
328 CaV1 localizations and a dense projection marker, in this case ELKS-Skylan-S (Figure 6A,B).
329 RyR localizations are diffusely distributed, and lateral to the dense projection (ELKS to RyR
330 center of mass distance: 393 nm; 25 synapses) (Figure 6C). RyR localizations are correlated
331 with CaV1 (RyR to CaV1 center of mass: 166 nm). Closer inspection of the images suggests
332 that RyR and CaV1 are often interdigitated in adjacent zones (Figure 6A). To characterize this
333 relationship, we performed a nearest neighbor analysis: 94% of RyR localizations are within
334 100nm of a CaV1 localization (Figure 6D). CaV1 exhibits a slightly broader distribution;
335 nevertheless, 82% of CaV1 localizations are within 100nm of a RyR channel. The spatial
336 correlation between CaV1 and RyR is consistent with the functional interactions observed by
337 physiology and electron microscopy at lateral sites, which is independent of CaV2.

338 **Different UNC-13 isoforms are associated with CaV1 and CaV2**

339 Vesicle docking and SNARE priming requires UNC-13 proteins. Null mutations in *unc-13*
340 nearly eliminate neurotransmission and vesicle docking in *C. elegans* (Hammarlund et al., 2007;
341 Richmond et al., 1999). We edited the *unc-13* locus at the common C-terminus to append
342 Skylan-S to all isoforms ('UNC-13all')(Extended Data 4D). Both CaV2 and CaV1 calcium
343 channels are tightly associated with UNC-13 (Figure 7A-C). Nearest-neighbor analysis indicates
344 that 99.7% of CaV2 channels are within 100 nm of an UNC-13 localization, and 89% of CaV1
345 channels are within 100 nm of an UNC-13 protein (Figure 7D).

346 The short isoform UNC-13S lacks the RIM-binding domain C2A, and has a diffuse
347 distribution at synapses (Hu et al., 2013; Weimer et al., 2006; Zhou et al., 2013). UNC-13S was
348 edited at its unique N-terminus to include a Skylan-S tag. UNC-13S does not colocalize with
349 CaV2 (peak-to-peak 319 nm) but is associated with CaV1 (Figure 8A-C). Nearest neighbor
350 analysis indicates that 99% of UNC-13S localizations are within 100nm of a CaV1 channel
351 (Figure 8D), demonstrating that a specialized isoform of UNC-13 docking machinery is localized
352 to CaV1 calcium channels.

353

354 **Discussion**

355 Calcium channel classes tend to be associated with specific tissue functions: CaV2 (N,
356 P/Q, R-type) with synaptic transmission, and CaV1 (L-type) channels with muscle contraction.
357 Here, we demonstrate that both CaV2 and CaV1 channels drive vesicle fusion at *C. elegans*
358 neuromuscular junctions and mediate the release of different synaptic vesicle pools. In
359 electrophysiological assays, these pools are genetically separable and perfectly
360 complementary. CaV2 channels fuse vesicles near the dense projection, whereas CaV1
361 channels drive vesicle fusion at lateral sites in the same synapses, as revealed by flash-and-
362 freeze electron microscopy. Super-resolution imaging indicates that CaV2 channels and the
363 active zone proteins Neurexin, α-Liprin, ELKS, and RIMBP are in tight 300 nm clusters at the
364 dense projection, and CaV2 is associated with the long isoform of the docking and priming
365 protein UNC-13L. By contrast, CaV1 is dispersed in the synaptic varicosity and is associated
366 with the short isoform UNC-13S. Finally, vesicle fusion mediated by CaV1 is dependent on the
367 ryanodine receptor, presumably by regulating calcium release from internal stores (Figure 9).

368

369 **CaV1 functions at synapses**

370 In *C. elegans* there is only a single L-type channel, encoded by the *egl-19* gene, which
371 primarily plays a role in muscle (Lee et al., 1997). EGL-19 also generates calcium action
372 potentials in some neurons (Liu et al., 2018), and thereby can substitute for the absence of
373 voltage-gated sodium channels in nematodes (Liu et al., 2018). However, L-type channel

374 inhibitors do not affect evoked release in motor neurons, but rather cause a decrease in the mini
375 rate (Tong et al., 2017). We demonstrate that null mutations in *egl-19* have reduced rates of
376 tonic miniature currents, are localized presynaptically, and are involved in fusions of a specific
377 sub-pool of synaptic vesicles. Together these data demonstrate that this L-type channel is
378 acting to mediate fusion of synaptic vesicles.
379
380 **Multiple calcium channels - coupling and voltage-dependence**
381 Based on physiological data alone, it was possible that CaV1 and CaV2 channels could
382 function at separate synapses. However, the electron microscopy and fluorescence
383 experiments demonstrate that these channels are localized and functioning at the same
384 synaptic varicosity. Participation of multiple classes of calcium channels at the same synapse
385 may function to tune the dynamics of neurotransmission. Differences in voltage-dependent
386 activation, inactivation, clustering, or distance to docked vesicles could regulate synchronous or
387 asynchronous release (Dolphin, 2021).
388
389 One important difference is that CaV1 channels inactivate more slowly than CaV2
390 channels and can therefore more accurately report synaptic depolarization (Naranjo, Wen, &
391 Brehm, 2015; Yu, Yuan, Westenbroek, & Catterall, 2018). For example, CaV1.3 and CaV1.4
392 mediate vesicle fusion in sensory neurons, and slow inactivation of these channels allows these
393 synapses to accurately report the depolarization status of the synaptic bouton (McRory et al.,
394 2004; Platzer et al., 2000). The *C. elegans* CaV1 channel EGL-19 also exhibits slow inactivation
395 *in vivo* (Lainé, Ségor, Zhan, Bessereau, & Jospin, 2014), which likely contributes to tonic
396 miniature currents in a graded fashion (Liu et al., 2018). Continued calcium influx through CaV1
397 may act to terminate neurotransmission in motor neurons; calcium influx through EGL-19 is
398 specifically coupled to repolarization via SLO-2 BK potassium channels (Liu et al., 2014).
399
400 The most profound difference for CaV1 and CaV2 channels at *C. elegans*
401 neuromuscular junctions is that they are differentially localized: CaV2 is localized to a large
402 cluster at the dense projection, CaV1 is distributed broadly in the synapse. Vesicle pools can be
403 assayed as tightly coupled or loosely coupled to calcium channels based on sensitivity to EGTA
404 (Dittman & Ryan, 2019; Eggermann et al., 2012). At *C. elegans* neuromuscular junctions, UNC-
405 13L mediates tight coupling (EGTA-insensitive), whereas UNC-13S mediates loose coupling
406 (EGTA-sensitive) (Hu et al., 2013). Consistent with these findings, UNC-13L is tightly coupled to
407 CaV2 channels at dense projections. CaV1 channels are dispersed across the synapse and
408 localizations are frequently solitary. Nevertheless, CaV1 channels can drive fusion across a
409 broad distribution of docked vesicles, extending 500 nm from the dense projection.

410

411 The requirement of CaV1 for the fusion of this distal pool of vesicles is likely to be
412 mediated by the ryanodine receptor rather than by CaV1 directly. Calcium influx from CaV1
413 channels stimulates the release of calcium from the endoplasmic reticulum via the ryanodine
414 receptor (Bouchard, Pattarini, & Geiger, 2003). In skeletal muscle, CaV1.1 is physically coupled
415 to RyR1 and voltage-sensing by the calcium channel can gate the ryanodine receptor in the
416 absence of extracellular calcium (Schneider, 1994). In neurons, it is not clear if ryanodine
417 receptor activation is physically coupled to CaV1 activation. In *C. elegans*, there is likely no
418 direct-physical link between CaV1 and RyR since depolarizations in the absence of calcium do
419 not elicit synaptic vesicle release (Liu et al., 2005). Nevertheless, our data indicate that these
420 channels are linked spatially and functionally. Nearest neighbor analysis indicates that
421 essentially all RyR localizations are within 100 nm of a CaV1 channel, and the electrophysiology
422 and electron microscopy demonstrate that they mediate fusion of the same pool of vesicles.
423

424 In contrast to CaV1, CaV2-mediated release is not dependent on RyR but rather is
425 potentiated by RyR. In the presence of CaV1 blockers, the frequency of miniature currents is not
426 decreased by loss of the RyR, indicating that CaV2 reliably drives vesicle fusion on its own.
427 Rather, it is the amplitude of the miniature current that is reduced in the absence of RyR. The
428 simplest interpretation is that calcium sparks from internal stores are directly acting to fuse
429 synaptic vesicles (Llano et al., 2000); however, we cannot exclude that potentiation is caused
430 indirectly by increases in basal cytosolic calcium at synapses. It is possible that increases in
431 global calcium are acting to increase the probability of vesicle fusion (Galante & Marty, 2003).
432

433 The participation of the CaV1 L-type channel EGL-19 in synaptic transmission in
434 *C. elegans* is unusual but not unprecedented. CaV1 channels also play a primary role in
435 synaptic vesicle fusion at graded sensory synapses: CaV1.3 drives neurotransmission in hair
436 cells and CaV1.4 acts at ribbon synapses in photoreceptors (Schmitz & Witkovsky, 1997;
437 Zhang, Robertson, Yates, & Everett, 1999). CaV1.2 and CaV1.3 are also expressed broadly in
438 the brain and function in dendritic spines during synaptic plasticity (Hell et al., 1996, 1993;
439 Nanou & Catterall, 2018). Ryanodine receptors are also found at vertebrate presynapses
440 (Bouchard et al., 2003), and potentiate release at GABA neurons in the cerebellum (Galante &
441 Marty, 2003). CaV1.3 is physically coupled to and activates RyR2 to release calcium stores in
442 cultured hippocampal neurons (Kim et al., 2007). Recent work indicates that CaV1 channels
443 and RyR2 must be colocalized to function together at cellular junctions in the cell body of
444 hippocampal neurons (Sahu et al., 2019).
445

446 Moreover, cooperation between CaV2 and CaV1 channels at synapses may be
447 widespread. Immunofluorescence experiments indicate that both CaV1 and CaV2 channels are
448 localized together at the same neuromuscular junctions in the fly (Krick et al., 2021), and mouse
449 CaV1 and CaV2 channels function together at neuromuscular junctions (Katz, Ferro, Weisz, &
450 Uchitel, 1996; Urbano & Uchitel, 1999). Pharmacological experiments suggest that CaV1 and
451 CaV2 channels may function together in GABA neurons in the central nervous system
452 (Goswami, Bucurenciu, & Jonas, 2012; Rey et al., 2020). Vertebrate homologs of the two worm
453 UNC-13 isoforms, Munc13-1 and bMunc13-2, function together at the same synapses (Kawabe
454 et al., 2017) and suggests that this organization of synapses into separately regulated pools of
455 synaptic vesicles may be general.
456

457 **Methods**

458 **Rescue of Lethal Calcium Channel Mutants**

459 Lethal CaV1 / *egl-19(st556)* animals were rescued by Mos-mediated transgenes
460 (*oxTi1047[Pset-18::egl-19b::let-858 3'utr] II*. EG9034 'CaV1 (Δns)') or by extrachromosomal
461 array (*oxEx2017[Pset-18::eGFP_egl-19b::let858utr ; Punc-122::GFP].* EG8827 'CaV1(Δns)
462 RyR(-)') (Frøkjær-Jensen et al., 2014, 2008). An *egl-19* minigene was constructed from cDNA
463 and portions of gDNA containing small introns to aid expression. The first exons 1-4 are cDNA,
464 followed by gDNA of exon 5-9, and cDNA of exon 10-17. The minigene was placed downstream
465 from a muscle P*set-18* promoter and inserted directly into the genome by MosSCI (Frøkjær-
466 Jensen et al., 2008).
467
468 For the array rescue of CaV1 in muscle, *Pset-18::eGFP_egl-19b::let858utr ; Punc-122::GFP*
469 was microinjected into the gonad of adult hermaphrodite *egl-19(n582) C. elegans.* Array positive
470 animals were selected and crossed with *egl-19(st556)* (RW3563), which rescued lethality but
471 lacked expression in the nervous system (EG8409). The resulting construct *oxTi1047* was
472 crossed into CaV1(-) / *egl-19(st556)* animals (RW3563), which rescued lethality but lacked
473 expression in the nervous system.
474
475 To demonstrate that phenotypes in this EG9034/EG8409 were due to loss of nervous system
476 function, we expressed the *egl-19* minigene under the neuron-specific P*snt-1* promoter and
477 inserted the construct into the genome by miniMos (Frøkjær-Jensen et al., 2014). The resulting
478 *oxTi1049* construct was crossed into the muscle-rescued CaV1(Δns) animals (EG9034) to
479 generate EG9145.
480
481 Lethal double mutants of CaV2-RyR (genotype: *unc-2 (lj1); unc-68 (e540)*) and CaV2-CaV1
482 (genotype: *unc-2 (lj1); egl-19 (st556)*) were rescued by an extrachromosomal array expressing
483 SNAP::CaV2/*unc-2* cDNA in a minimum set of acetylcholine head neurons, using a previously
484 described truncated *unc-17* promoter, referred to as 'P*unc-17*h' (Hammarlund et al., 2007;
485 Topalidou et al., 2016). The extrachromosomal array *oxEx2096* was generated in the *unc-2(lj1)*
486 strain AQ130 and crossed to RyR / *unc-68(e540)* or CaV1 / *egl-19(st556) oxTi1047[*P*set-*
487 *18::egl-19b]* animals to generate double mutants. The resulting strains are lethal without the
488 presence of *oxEx2096[*P*unc-17h*::*SNAP*::*unc-2]* and were used in electrophysiology
489 experiments.
490

491 **Behavioral Experiments**

492 Animals were maintained under standard laboratory conditions. For behavioral experiments, 3

493 to 6 well-fed, young adult worms were transferred to a 10cm containing standard NGM. Each
494 assay was recorded for 5 minutes at 8 frames per second using the worm tracking software
495 WormLab (2019.1.1, MBF Bioscience). The trajectory of each worm was collected using
496 WormLab and imported into custom written R scripts for analysis. Worms that crawled out of the
497 field of view during the first 3 minutes were discarded from analysis. Worms whose speed was
498 lower than 100um/s were excluded as they may have been damaged during transfer, the
499 number of worms that fell in this category were few and not different between groups. A reversal
500 was defined as backwards locomotion that lasted more than 4 frames or 500ms.
501
502 **Generation of CaV2::HALO by CRISPR/cas9**
503 CaV2 was tagged by CRISPR-mediated insertion of HALO coding DNA into the *unc-2*
504 endogenous genomic locus. A DNA mix containing 1) PCR-generated DNA repair template that
505 includes the HALO tag with an embedded *Cbr-unc-119(+)* cassette flanked by loxP sites and
506 33bp homology arms to the cut site, 2) plasmid DNA that directs expression of Cas9 and an
507 sgRNA (Schwartz & Jorgensen, 2016), and 3) an inducible negative selection plasmid directing
508 expression of a histamine-gated chloride channel in neurons, pNP403 (Pokala, Liu, Gordus, &
509 Bargmann, 2014) was injected into the gonads of young adult EG6207 *unc-119(ed3)* animals
510 (Maduro & Pilgrim, 1995; Schwartz & Jorgensen, 2016; Zhang et al., 2015). Transgenic animals
511 were selected for expression of *unc-119(+)*, and extrachromosomal-array bearing animals were
512 selected against by addition of histamine to the media. The *loxP::Cbr-unc-119(+)::loxP* region of
513 the insertion was excised by injecting pDD104[Peft-3::Cre] and identifying *unc-119(-)* animals
514 (Dickinson, Ward, Reiner, & Goldstein, 2013). The modified locus introduces HALO-tag within
515 an unconserved region in the second extracellular loop of CaV2 encoding UNC-2a. The
516 resulting strain EG9823 (genotype: *unc-119*(ed3); *unc-2*(ox672[HALO])) was subsequently used
517 to generate CRISPR-mediated insertions of SkylanS tags.
518
519 **Generation of Super-Resolution Tags by CRISPR/cas9**
520 Tags for other genes, including *egl-19, unc-68, elks-1, nrx-1, rimb-1, elks-1, syd-2, syd-1, magi-*
521 *1, ctn-1, unc-13,* and *unc-13b* were constructed as previously described (Schwartz &
522 Jorgensen, 2016). A single plasmid containing sgRNA and the repair template, composed of
523 57bp homology arms and SkylanS (Zhang et al., 2015) containing a *loxP::Cbr-unc-119(+)::loxP*,
524 was appended by SapTrap plasmid assembly. Each assembled plasmid was mixed with
525 plasmids to express Cas9 in the germline, and HisCl- in neurons, and injected into the gonads
526 of young adult EG9823 animals. After selecting for *unc-119(+)* and selecting against
527 extrachromosomal arrays by histamine application, animals were injected with
528 pDD104[P*eft-3::Cre*], selected for excision of *loxP::Cbr-unc-119(+)::loxP*, and outcrossed once

529 before analysis by super-resolution microscopy.

530

531 **Strains:**

532 All strains were maintained at 22°C on standard NGM media seeded with OP50.

Name	Strain	Genotype
Wild-type	N2	*wild-type*
CaV2(-)	AQ130	*unc-2(lj1) X*
RyR(-)	CB540	*unc-68(e540) V*
CaV1(-) balanced	RW3563	*egl-19(st556) / unc-82(e1323) unc-24(e138am) IV*
EM Wildtype	EG5793	*oxSi91*[*Punc-17::ChIEF::mCherry::unc-54UTR unc-119(+)*] *II; unc-119(ed9) III*
EM CaV2(-)	EG6584	*oxSi91[Punc-17::ChIEF::mCherry::unc-54UTR unc-119(+)*] *II; unc-2(lj1) X*
EM CaV1(-)	EG6585	*oxSi91[Punc-17::ChIEF::mCherry::unc-54UTR unc-119(+)*] *II; egl-19(n582) IV*
EM CaV2(-) CaV1(-)	EG6586	*oxSi91[Punc-17::ChIEF::mCherry::unc-54UTR unc-119(+)*] *II; egl-19(n582) IV; unc-2(lj1) X.*
EM RyR(-)	EG6587	*oxSi91[Punc-17::ChIEF::mCherry::unc-54UTR unc-119(+)*] *II; unc-68(e540) V*
CaV1 muscle rescue array	EG8409	*egl-19(st556) IV; egl-19(oxEx2017[Pset-18::eGFP_egl-19b::let-858-utr ; ccGFP])*
CaV1(Δns) RyR(-)	EG8827	*egl-19(st556) IV; unc-68(e540) V; oxEx2017[Pset-18::eGFP::egl-19b::let-858-utr;* P*unc-122::GFP]*
CaV1(Δns)	EG9034	*oxTi1047[Pset-18::egl-19b::let-858-3'utr] II; egl-19(st556)*
CaV2(Δnmj) RyR(-)	EG9405	*unc-68(e540) V; unc-2(lj1) X; oxEx2097[Punc-17h::SNAP::unc-2]*
CaV2(Δnmj) CaV1(Δns)	EG9406	*unc-2(lj1) oxTi1047[Pset-18::egl-19b::let-858 3'utr] II; egl-19(st556)IV; unc-2(lj1) X; oxEx2097[Punc-17h::SNAP::unc-2]*
RIMBP-SKYS CaV1-HALO (+ns rescue) Giant Ankryin-SNAP	EG9418	*egl-19(st556) IV; ox704[skylan-s::rimb-1] III; oxTi1047[Pset-18::egl-19b::let-858utr; HygroR(+)], oxTi1055[Psnt-1::HALO::egl-19b; NeoR(+)] II; unc-44(ox708[unc-44::snap]) IV*
CaV2-HALO Liprinα-SKYS	EG9425	*unc-119(ed3) III; unc-2(ox672[HALO]), syd-2(ox715[skylan-s(loxP::Cbr-unc-119(+)::loxP)]) X*
RIMBP-SKYS CaV2-HALO CaV1-SNAP	EG9475	*oxIs322[Cbr-unc-119(+)* P*myo-2::mCherry::histone* P*myo-3::mCherry::histone] II; unc-119(ed3) III; rimb-1(ox704[skylan-s]) III; egl-19(ox728[snap]) IV; unc-2(ox672[HALO::]) X*
αCatulin-SKYS CaV1-SNAP CaV2-HALO	EG9476	*ctn-1d(ox727[skylan-s]) I; oxIs322[Cbr-unc-119(+)* P*myo-2::mCherry::histone* P*myo-3::mCherry::histone] II; unc-119(ed3) III; egl-19(ox728[SNAP]) IV; unc-2(ox672[HALO]) X*
NRX-SKYS CaV1-SNAP CaV2-HALO	EG9588	*egl-19(ox728[SNAP]) IV; nrx-1(ox719[skylan-s]) V; unc-2(ox672[HALO]) X*
ELKS-SKYS CaV1-SNAP CaV2-HALO	EG9617	*elks-1(ox747[skylan-s]), egl-19(ox728[SNAP]) IV; unc-2(ox672[HALO]) X*

ELKS-SKYS CaV1-SNAP RyR-HALO	EG9667	*egl-19(ox728[SNAP]), elks-1(ox747[skylan-s]) IV; unc-68(ox721[HALO]) V*
Giant Ankryin -SKYS CaV1-SNAP CaV2-HALO	EG9722	*unc-2(ox672[HALO]) X; egl-19(ox728[SNAP]) IV; unc-44(ox802[skylan-s]) IV*
UNC13all-SKYS CaV1-SNAP CaV2-HALO	EG9723	*unc-2(ox672[HALO]) X; egl-19(ox728[SNAP]) IV; unc-13(ox748[skylan-s]) I*
UNC13short-SKYS CaV1-SNAP CaV2-HALO	EG9782	*unc-13(ox814[SKYLAN-S(loxP)]) I; unc-2(ox672[HALO]) X; egl-19(ox728[SNAP]) IV*
CaV2-HALO	EG9823	*unc-2(ox672[HALO::unc-2]) X; unc -119(ed3) III*
RIMBP-SKYS CaV1-HALO(+ns rescue) Lin7-SNAP	EG10094	*oxTi1055[Psnt-1::HALO::egl-19b; NeoR(+)] oxTi1047[Pset-18::egl-19b::let858utr; HygroR(+)] II; unc-119(ed3) rimb-1(ox704[skylan-s]) III; egl-19(st556) IV ; oxEx2223[Punc-129::lin-7::SNAPf-tag]*
SYDE-SKYS CaV2-HALO	EG10095	*syd-1(ox723[skylan-s(loxP::Runc-119::loxP)]) II; unc-119(ed3) III; unc-2(ox672[HALO]) X*
MAGI-SKYS CaV1-SNAP CaV2-HALO	EG10096	*unc-119(ed3) III; egl-1-19(ox728[snap]), magi-1(ox755[skylan-s(loxP::Cbr-unc-119::loxP)]) IV; unc-2(ox672[HALO]) X*

Single Molecule Localization Microscopy

Super-resolution images were recorded with a Vutara SR 352 (Bruker Nanosurfaces, Inc., Madison, WI) commercial microscope based on single molecule localization biplane technology (Juette et al., 2008; Mlodzianoski, Juette, Beane, & Bewersdorf, 2009). *C. elegans* expressing HALO- tagged proteins (Encell, 2013; Mollwitz et al., 2012) were stained for two hours in 50μM of HTL-JF646, and 50μM of STL-JF549cp, STL-JF549, or STL-JF549pa (Gift from Luke Lavis, Janelia Farms; (Grimm et al., 2017, 2015)). Early super-resolution experiments were conducted with JF549-STL or PA-JF549-STL, we later found that a new cell permeable variant cp-JF549-STL improved labeling of channels. Animals were recovered 12 hours at 15degC on agar seeded with OP50 bacteria. Live intact animals were anesthetized in 25mM NaN3 and regions of their dorsal cords that were positioned directly against the cover glass and away from the intestine were imaged with 640nm excitation power of 10kW/cm2, or 549nm excitation power of 5kW/cm2 SkylanS was imaged by 488nm excitation at 2kW/cm2, while photoactivated by 0.37mW/cm2 405nm light. Images were recorded using a 60x/1.2 NA Olympus water immersion objective and Hamamatsu Flash4 V1 sCMOS, or 60x/1.3 NA Silicon immersion objective and Orca Fusion BT SCMOS camera with gain set at 50 and frame rate at 50 Hz. Data was analyzed by the Vutara SRX software (version 7.0.0rc39). Single molecules were identified by their brightness frame by frame after removing the background. Identified molecules were localized in three dimensions by fitting the raw data in a 12x12-pixel region of interest centered

553 around each particle in each plane with a 3D model function that was obtained from recorded
554 bead data sets. Fit results were filtered by a density based denoising algorithm to remove
555 isolated particles. The experimentally achieved image resolution of 40nm laterally (x,y) and 70
556 nm axially (in z) was determined by Fourier ring correlation. Localizations were rendered as
557 80nm.
558
559 **SML Analysis**
560 Localization data was exclusively collected from the dorsal nerve cord, which contains axons
561 and synapses but no neuronal soma. We performed a 3D reconstruction of C. elegans dorsal
562 nerve cord to inform region of interest selection from fluorescent images. The orientation of
563 dorsal cord synapses is predictable. Excitatory acetylcholine neurons and inhibitory GABA
564 neurons synapse onto muscle arms (Figure 3A). These connections are near the edges of the
565 cord bundle. Thus, the roll of the animal affects the orientation of the synapse; en face or axial.
566 For single molecule localization experiments, animals were rolled to ensure en face orientation
567 of synapses. Synapses that were in focus and en face were analyzed. The average size of a
568 synapse from the dorsal nerve cord is 579.7nm (SEM +/- 16nm). Thus, super-resolution
569 analysis regions of interest were narrowed to localizations within 700nm of the dense projection
570 marker. Localization position data was flattened in the z-dimension due to chromatic
571 aberrations. A script was used to calculate the center of each probe. To compare the distribution
572 of probe A to probe B, an angle between the two clusters centers was calculated. The
573 distribution distances were calculated by measuring the distance along the center-to-center axis
574 from a probe B to the center of cluster A, and cluster B. Nearest neighbor analysis was done
575 with knnsearch(). The 95% confidence interval of these distance measurements is considered
576 the diameter of the cluster. Distribution center and range or “diameter” were reported as (mean ,
577 95%CI). Proberuler available at https://github.com/bdmscience/proberuler
578
579 **Electrophysiology**
580 All electrophysiological experiments were completed with young adult hermaphrodites. The
581 animals were immobilized and dissected as previously described (Ping Liu, Chen, Mailler, &
582 Wang, 2017). Worm preparation was bathed with an extracellular solution containing (in mM)
583 NaCl 140, KCl 5, CaCl2 0.5, MgCl2 5, dextrose 11 and HEPES 5 (pH 7.2). Spontaneous
584 postsynaptic currents (PSCs) at neuromuscular junction were recorded at a holding voltage
585 of -- 60 mV with a pipette solution containing (in mM) KCl 120, KOH 20, Tris 5, CaCl2 0.25,
586 MgCl2 4, sucrose 36, EGTA 5, and Na2ATP 4 (pH 7.2). The classic whole-cell recordings were
587 performed with a Multiclamp 700B amplifier (Molecular Devices, Sunnyvale, CA, USA) and the
588 Clampex software (version 10, Molecular Devices). Data were filtered at 2 kHz and sampled at

589 10 kHz. Nemadipine-A (Sigma-Aldrich) was first dissolved in DMSO to make frozen stock
590 solution (10mM), and was diluted to a final concentration of 10 μM in extracellular solution
591 before use. Animals were treated for 5 minutes. The frequency and amplitude of minis were
592 quantified with MiniAnalysis (Synaptosoft, Decatur, GA, USA). The amplitudes of evoked
593 currents were quantified using Clampfit (version 10, Molecular Devices, Sunnyvale, CA, USA)
594
595 **Quantal Modelling**
596 A 5-term gaussian distribution was fit to cumulative frequency distribution of amplitudes per
597 condition in 1pA bins using MATLAB Curve Fitter (Mathworks, Natick, MA, USA). The terms
598 were centered on 9 +/- 2 pA intervals which represent the mode of amplitudes; a single
599 quantum. (del Castillo & Katz, 1954). The coefficient for the mean of the first gaussian curve
600 was set to the mode amplitude (9 pA+-2). Every coefficient for subsequent gaussian terms were
601 set to 9pA+-2 intervals, but the other coefficients were not constrained and allowed to find a
602 best fit. Area under each curve was calculated using MATLAB trapz().
603
604 **Flash and Freeze Electron Microscopy**
605 Electron microscopy was performed as previously described (Watanabe et al., 2013).
606 Freezing was performed on a Leica EMpact2 (Leica, Wetzlar, Germany). To stimulate
607 neurotransmission animals were exposed to blue (488nm) LED light for 20ms and frozen 50ms
608 later. 33nm serial sections were taken and imaged using a Hitachi H-7100 transmission electron
609 microscope equipped with a Gatan Orius digital camera (Gatan, Pleasanton, CA). Micrographs
610 were analyzed in ImageJ using a program for morphological analysis of synapses (Watanabe,
611 Davis, Kusick, Iwasa, & Jorgensen, 2020). Scripts available at:
612 https://github.com/shigekiwatanabe/SynapsEM
613
614 **Dorsal Nerve Cord Reconstruction**
615 Serial sections were cut at 100nm and imaged using JEOL JEM-1400 (JEOL, Peabody, MA)
616 then annotated and assembled using TrackEM2 in FIJI (Cardona et al., 2012). Specifically, a
617 wireframe was fit through each process that was suspected to be in the previous micrograph.
618 Then an outline of the plasma membrane of each process was drawn. We analyzed several
619 criteria to more specifically determine the specific process name and type: the morphology of
620 each process and compared to previously published data (J.G. White, E. Southgate, J.N.
621 Thomson, & S. Brenner, 1986), and the number of synapses. These data allow us to determine
622 the identity of a process with some certainty.
623
624 **Acknowledgements**

We thank Lexy von Diezmann for development of Proberuler. We thank Luke Lavis for providing all Janelia Fluor dyes (JF Dyes). Wayne Davis suggested using the early expressing *set-18* promoter to rescue CaV1. We thank the University of Utah Fluorescence Imaging Core for instrumentation, and the Caenorhabditis Genetics Center (CGC) for maintaining and distributing strains to the *C. elegans* community. We thank Patrick McEachern, Matthew Rich, Jessica Vincent and M. Wayne Davis for their critical reviews of this manuscript. EMJ is an investigator at Howard Hughes Medical Institute.

FUNDING

Erik Jorgensen

National Science Foundation NeuroNex 2014862

National Institute of Health NIH NINDS R01 NS034307

Sean Merrill

NIH F31 NRSA Predoctoral Fellows grant F31 NS084826

Zhao-wen Wang

National Institute of Health NIH R01 MH085927 and R01 NS109388

Andres Villu Maricq

National Institute of Health NIH R01 NS094421

Author Contributions

BDM SAM EMJ Wrote manuscript

SAM SW BDM ZWW EMJ Designed experiments

SAM SW EMJ Conceived of the project

PMC AVM Performed behavioral recording and analysis

PL Performed electrophysiology

BDM PL Analyzed electrophysiology data

SAM BDM Performed single molecule localization microscopy

BDM LVD designed Proberuler

BDM SAM Analyzed single molecule localization data

SAM AC Performed genetic crosses

SAM AC BDM cloned plasmids

SAM BDM Generated transgenic animals

SW Performed and analyzed time resolved electron microscopy

BDM AS MS annotated serial reconstruction

AS MS Performed serial reconstruction electron microscopy

663 **Table 1: Super-resolution Alleles Generated for this study.**

664

Allele	Gene	Common name	sgRNA	Repair template	Tag	Chr	Terminus
ox672	*unc-2*	CaV2	pSAM429 (ACAGACCGCCAACCAACCGG)	pSAM593	HALO	X	internal
ox704	*rimb-1*	RIMBP	TGGGTAAATCGATAAATCG	pSAM514	SKY-S	III	c
ox719	*nrx-1*	Neurexin	TTTTCTTTGCCACCCCATTC	pSAM534	SKY-S	V	c
ox721	*unc-68*	RyR	pSAM488 (gattagttagttccaagaaA)	pSAM593h	HALO	V	n
ox727	*ctn-1d*	α-Catulin	CATCCAATGTAATCGGC	pSAM598	SKY-S	III	c
ox728	*egl-19*	CaV1	CTTCTCATCCATTGCTC	pSAM604	SNAP	IV	internal
ox729	*syd-1*	SYDE	GCACTGCGATTCCGAGACAT	pSAM545	SKY-S	II	c
ox730	*syd-2*	α-Liprin	TTGCTGTAGCTCATatttct	pSAM549	SKY-S	X	n
ox747	*elks-1*	ELKS/CAST	gagcagtacaatATGGCACC	pSAM550	SKY-S	IV	n
ox748	*unc-13all*	UNC13all	gctttgaatccaacaaaaaa	pSAM613	SKY-S	I	c
ox803	*magi-1*	MAGI	aagATGACCGACAAAACAGC	pSAM552	SKY-S	IV	n
ox814	*unc-13b*	UNC13s	GGAACTGCAAGACTTGGCAC	pSAM684	SKY-S	I	n
ox802	*unc-44*	Giant Ankyrin	GCTGTTGGTCGTGCTCCCGA	pSAM546	SKY-S	IV	c
ox708	*unc-44*	Giant Ankyrin	GCTGTTGGTCGTGCTCCCGA	pSAM557	SNAP	IV	c

665

666 **Table 2: Common names and nomenclature used in this study**

Common name	Mammalian ortholog	*C. elegans* ortholog	*Drosophila* ortholog
CaV2	CaV2.1 CaV2.2 CaV2.3	UNC-2	Cacophony
CaV1/L-type	CaV1.1 CaV1.2 CaV1.3 CaV1.4	EGL-19	DmCa1D
ELKS	ELKS/CAST	ELKS-1	Bruchpilot
RyR	RYR1 RYR2 RYR3	UNC-68	dRyr
UNC13all	Munc13-1 ubMunc13-2 bMunc13-2 Munc13-3	UNC-13L, UNC-13S	Unc13A Unc13B
UNC-13S	bMunc13-2 Munc13-3	UNC-13S	UNC13B
RIMBP	RIMBP	RIMB-1	Rbp
Veli/LIN7	LIN7A	LIN-7	Lin-7
Giant Ankyrin	gAnkB	UNC-44L	AnkG

Neurexin/NRX	Neurexin 1	NRX-1	DNrx
α-Liprin	α-Liprin	SYD-2	Liprin-α
SYDE	SYDE	SYD-1	Syd-1
α-Catulin	α-Catulin	CTN-1	α-Cat
MAGI1	MAGI1	MAGI-1	Magi

667

668 **Table 3: Summary of strain nomenclature and alleles**

Common name	Usage	CaV2	CaV1	RyR	CaV2 rescue	CaV1 rescue
Wildtype N2 Bristol	ePhys EM behavior	wt	wt	wt	n/a	n/a
CaV1(rescue)	behavior SMLM	wt	*st556*	wt	n/a	*oxTi1047[Pset-18::egl-19b] oxTi1049[Psnt-1::HALO::egl-19b]*
CaV1(Δns)	behavior ePhys	wt	*st556*	wt	n/a	*oxTi1047[Pset-18::egl-19b]*
CaV1(Δns) RyR(-)	ePhys	wt	*st556*	e540	n/a	*oxEx2017[Pset-18::eGFP::egl-19b]*
CaV2(Δnmj) CaV1(Δns)	ePhys	*lj1*	*st556*	wt	oxEx2096[P*unc-17h*::*SNAP*::*unc-2*]	*oxTi1047[Pset-18::egl-19b]*
CaV2(Δnmj) RyR(-)	ePhys	*lj1*	wt	*e540*	oxEx2096[P*unc-17h*::*SNAP*::*unc-2*]	n/a
CaV2(-)	ePhys EM	*lj1*	wt	wt	no	n/a
RyR(-)	ePhys EM	wt	wt	*e540*	n/a	n/a

CaV1(-) CaV2(-)	EM	*lj1*	*n582*	wt	no	no
CaV1(-)	EM	wt	*n582*	wt	n/a	no

Figure 1. nervous system CaV1 is required for normal behavior and locomotion.
(A) Viability of calcium channel double mutants.
(B) Worm Tracks. Healthy animals were tracked for 5 minutes with a frame rate of 8 frames per second. The path the animal created was plotted, starting point is indicated, asterisks represent reversal events.
(C) Total average distance animals travelled per animal during the 5-minute interval by genotype. Wild-type 71.2 ±9.5 mm. CaV1(Δns) 39.0 ±1.8 mm. CaV1(Δns) +rescue 74.4 ±10.5 mm.
(D) Average speed, including both forward and backward bouts but excluding pauses, for the duration of the assay. Wild-type 294.9 um/s ± 19.4 um/s. CaV1(Δns) 133.8 um/s ± 6.3 um/s. CaV1(Δns) +rescue 331.7 um/s ± 13.3 um/s.
(E) Average distance of forward locomotion between reversal events that animals travelled by genotype. Wild-type 12.2 mm ±2.0 mm. CaV1(Δns) 17.7 mm ±1.7 mm. CaV1(Δns) +rescue 15.3 mm ± 4.0 mm.
(F) Average duration of forward run between reversal events. Wild-type 41.9 ± 8 s. CaV1(Δns) 14.1 ± 1.3 s. CaV1(Δns) +rescue 46.2 ± 10.5 s.
(G) Average number of reversal events per minute exhibited by animals by genotype. Wild-type 1.9 ± 0.3 events. CaV1(Δns) 3.8 ± 0.5 events. CaV1(Δns) +rescue 1.3 ± 0.3 events.
(H) Average distance travelled in reverse per animal by genotype. Wild-type 601.9 ± 65.1 um. CaV1(Δns) 413.2 ± 56.8 um. CaV1(Δns) +rescue 1026 ± 111.1 um.
(I) Average duration of reversal run. Wild-type 2.2 +- 0.1 s. CaV1(Δns) 2.4 +/- 0.2 s. CaV1(Δns) +rescue 2.5 +- 0.2 s.
Wild-type n=11, CaV1(Δns) n=16, CaV1(Δns) +rescue n=13. Error bars reported in SEM. Genotypes were blinded. One-way ANOVA with Tukey's multiple comparisons was used to calculate p-value. *$p<0.05$, **$p<0.005$, ***$p<0.001$, ****$p<0.0005$
Data available as Source Data 1

697 **Figure 2. CaV2 and CaV1-RyR fuse different vesicle pools.**
698 (A) Spontaneous miniature currents mediated by CaV1 and RyR are inhibited by nemadipine.
699 Wild-type: 32.2 ± 2.1 minis/s n=8, wild type with nemadipine (10 μM): 18.4 ± 2.1 mini/s n=8.
700 CaV1(Δns): 18.7 ± 3.1 minis/s n=9, with nemadipine 19.1 ±2.7 mini/s n=6. RyR(-): 20.9 ± 1.5
701 minis/s n=7, with nemadipine 20.7 ±1.3 mini/s n=7. CaV2(-): 18.7 ± 3.5 minis/s n=7, with
702 nemadipine 1.7 ± 0.6 mini/s n=9. One-way ANOVA with Dunnett's multiple comparisons test
703 and one-way ANOVA with Tukey's multiple comparisons tests were used to calculate
704 significance.
705 (B) The ryanodine receptor mediates large amplitude tonic miniature currents. Wild type 22.3 ±
706 1.9 pA n=8, wild type with nemadipine 22.6 ± 2.1 pA n=8. CaV2(-): 22.1 ± 3.5 pA n=7, CaV2(-)
707 with nemadipine 24.1 ± 3.4 pA n=9. CaV1(Δns): 23.4 ± 3.1 pA n=9, CaV1(Δns) with nemadipine
708 29.4 ± .9 pA n=6. RyR(-): 15.5 ± 0.6 pA n=7, RyR(-) with nemadipine 14.0 ± 0.9 pA n=7. One-
709 way ANOVA with Dunnett's multiple comparisons test and Welch's t-test were used to calculate
710 significance.
711 (C) Sample traces of spontaneous release in 0.5mM extracellular calcium.
712 (D) Cumulative distribution plot of miniature current amplitudes.
713 (E) Frequency distribution of mini amplitudes of wild-type and ryanodine mutants ± nemadipine,
714 normalized to modal value.
715 (F) Quantal analysis of post-synaptic amplitudes from wild-type ± nemadipine. The cumulative
716 plot of mini amplitudes was replotted into 1 pA bins and a single quantal mini amplitude
717 distribution was fit with a gaussian at a modal value of 9 ±2 pA. The wild-type distribution of
718 amplitudes was fit with a 5-term convolution of a single quanta (khaki-colored curve). 1-quanta
719 (rust) accounted for 36.2% of fusions. 2-quanta (butterscotch) 28.03%. 3-quanta (violet) 7.64%.
720 4-quanta (green) 5.42%. 5 or more quanta (blue) 21.45%.
721 (G) Quantal analysis of post-synaptic amplitudes from RyR(-) ± nemadipine animals. A 5-term
722 gaussian model was fit to the cumulative frequency of amplitudes 1pA bin size (peach). 1-
723 quanta (rust) accounted for 67.7% of fusions. 2-quanta (butterscotch) 25.1%. 3-quanta (violet)
724 0.2%. 4-quanta (green) 5.4%. 5 or more quanta (blue) 3.4%.
725 For all recordings, Vm = -60 mV, 0.5 mM calcium. Error bars reported in SEM. *p<0.05,
726 **p<0.005, ***p<0.001, ****p<0.0005. Data available as Source Data 2
727

728 **Figure 2, Extended Data. The ryanodine receptor acts in parallel to CaV2.**
729 (A) CaV2 and CaV1-RyR contribute additively to tonic release. Muscles were voltage-clamped,
730 and tonic miniature synaptic currents recorded in 0.5 mM extracellular calcium: wild type: 33 ±4
731 minis/s, n=8; CaV2(-): 19 ±4 minis/s n=7, CaV1(Δns): 21 ± 3 minis/s n=7, RyR(-): 20 ±4 minis/s
732 n=9. CaV2(Δnmj) RyR(-): 11 ± 2 minis/s n=7, CaV2(Δnmj) CaV1(Δns): 13 ±2 minis/s n=7,
733 CaV1(Δns) RyR(-): 20 ±2 minis/s n=7. Welch's t-test was used to calculate significance
734 (B) RyR is required for large-amplitude spontaneous events. At 0.5mM calcium, wild-type
735 23 ±2 pA n=8, and CaV2(-): 23 ±2 pA n=7, CaV1(Δns): 21 ±1 pA n=7, RyR(-): 16 ±2 pA n=9.
736 CaV2(Δnmj) RyR(-): (38 ±3 pA n=7, CaV2(Δnmj) CaV1(Δns): 26 ±3 pA n=7, and CaV1(Δns)
737 RyR(-): 17 ±2 pA n=7. Welch's t-test was used to calculate significance.
738 (C) Cumulative distribution plot of mutant amplitudes.
739 (D) Frequency distribution plot of voltage-gated calcium mutants amplitudes normalized to the
740 mode.
741 (E) Frequency distribution plot of ryanodine mutants with reduced amplitudes, normalized to
742 mode.
743 Error bars reported in SEM. *p<0.05, **p<0.005, ***p<0.001, ****p<0.0005

744 Data available as Source Data 2

745 **Figure 3. CaV2 and CaV1-RyR act at distinct vesicle release sites.**
746 (A-B) Docked vesicles (black arrows) are present near dense projections in electron micrograph
747 of unstimulated animals, but are reduced 50ms after channelrhodopsin stimulation.
748 (C) Interpretation of docking histograms. The number of synaptic vesicles that fuse due to
749 stimulation can be determined by comparing the number of synaptic vesicles docked within the
750 active zone without or with stimulation.
751 (D-H) Average number of docked vesicles per synapse at a given distance from the dense
752 projection with, or without light stimulation of channelrhodopsin.
753 (D) Wild-type animals exhibit fewer docked vesicles at all locations after stimulation. Wild type
754 (no stimulation), n=26 synapses. Wild type (stimulated) n = 24 synapses.
755 (E) The CaV2 null mutant *unc-2(lj1)* fuses vesicles greater than 33 nm from the dense projection
756 but not docked vesicles directly adjacent to the dense projection. CaV2(-) (no stimulation) n=14,
757 CaV2(-) (stimulated) n=27 synapses.
758 (F) The CaV1 hypomorphic mutant *egl-19(n582)* exhibits reduced fusions at all distances.
759 CaV1(-) (no stimulation) n=29 synapses. CaV1(-) (stimulated) n=16 synapses.
760 (G) The RyR mutant *unc-68(e540*) exhibits fusions adjacent to the dense projection, but lacks
761 fusions of lateral vesicles. RyR(-) (no stimulation) n=11 synapses. RyR(-) (stimulated) n=17
762 synapses.
763 (H) The double mutant CaV1 *egl-19(n582)* and CaV2 *unc-2(lj1)* lack fusion of all docked
764 vesicles after stimulation. CaV2(-) CaV1(-) (control) n=24 synapses. CaV2(-) CaV1(-)
765 (stimulated) n=17 synapses. Errors given in SEM, N = 2 animals for each condition.
766 Micrographs were segmented blind to treatment and genotype.
767 Data available as Source Data 3

768 **Figure 4. Dorsal nerve cord reconstruction and candidate dense projection markers.**
769 (A) 20-micron reconstruction of the wild-type *C. elegans* dorsal nerve cord. Dense projections are
770 highlighted to compare to superresolution images below. Scale bar 1um, section thickness 100 nm.
771 (B) CaV2 colocalizes with cytomatrix active zone proteins. Super-resolution images of Skylan-S-
772 tagged cytomatrix protein homologs in *C. elegans* NRX-1, RIMB-1, SYD-2, SYD-1, MAGI-1, CTN-1,
773 ELKS-1 compared to CaV2-HALO in the same animal.
774 (C) ELKS and CaV2 clusters form approximately 1 / um along the dorsal nerve cord from super-
775 resolution image analysis. Clusters were quantified for over dorsal nerve cords with an average
776 length of 17.8um, N= 8 animals
777 (D) Localization plot tool (Proberuler) example diagram of a single ELKS (cyan) and CaV2
778 (magenta) synapse. Cluster centers are marked by solid lines.
779 Data available as Source Data 5
780

781 **Figure 4, Extended Data. Tagging sites for calcium channels and UNC-13**.
782 (A-C), Tagging strategies and sites used for CRISPR/Cas9 tagging of the endogenous loci for
783 CaV2, CaV1, and RyR. Regions with low conservation were targeted for insertion of tags into
784 the genomic locus of each gene, *unc-2*, *egl-19*, and *unc-68*, respectively.
785 (D) Tagging strategy at the endogenous locus of *unc-13* CRISPR / Cas9. The C-terminal tag
786 labels all isoforms of UNC-13. The N-terminal tag labels the UNC-13S isoform. In addition, it will
787 label a rare transcript UNC-13-LMR (~2% of transcripts), that includes the C2A domain,
788 sequences upstream of UNC-13S, and all sequences included in UNC-13S (wormbase.org
789 version ws284).
790

Figure 5. CaV1 is excluded from the dense projection, and dispersed in the active zone.
(A, B) Localization microscopy plots of the dorsal nerve cord. ELKS is tagged with Skylan-S. The CaV2-HALO ligand is HTL-JF646, and the CaV1-SNAP tag ligand is STL-JF549pa.
(A) CaV2 (magenta) colocalizes with dense projections labeled with ELKS (cyan). CaV1-SNAP (yellow) is largely excluded from the dense projection; and scattered in the synaptic varicosity. Scale bar = 1um.
(B) Distributions of CaV2 and CaV1 in a synapse. Dense projections labeled with ELKS (cyan) colocalize with CaV2 (magenta), but not CaV1 (yellow). Scale bar = 250nm.
(C) Quantitation of protein localizations from multiple synapses. The center of mass of localizations was calculated from 2D plots. An axis between the centers was fixed and all localizations collapsed onto the axis. Localizations were combined into 33 nm bins, to match the electron microscopy analysis, and plotted as the fraction of total localizations. Data were collected and combined from n=26 synapses, N=5 animals. Data available as Source Data 5

Figure 5, Extended Data. Tagged CaV1 expressed in neurons forms clusters at presynaptic boutons.

Comparison of endogenously-tagged CaV1 and neuronally expressed rescue of CaV1.

(A) Endogenous CaV1 tag: Localization microscopy images of dorsal nerve cord with CaV1-SNAP stained with STL-JF549cp (yellow), CaV2-HALO stained with HTL-JF646 (purple), and Giant Ankyrin-SkylanS (red). scale bar = 1um.

(B) Exogenous CaV1 in the CaV1(Δns) strain. In the CaV1(Δns) background, CaV1 was rescued in neurons using a single copy transgene insertion of P*snt-1* promoter driving CaV1-HALO in neurons. Localization microscopy images of dorsal nerve cord. Dorsal cord of animals labelled with neuronal CaV1-HALO stained with HTL-JF646 (purple), Giant Ankyrin-SNAP stained with TMR-Star (red) and RIMBP-SkylanS (cyan). scale bar = 1um.

(C) Neuronal CaV1 colocalizes with Veli/LIN7 expressed in acetylcholine neurons. In the CaV1(Δns) background, CaV1 was rescued in neurons using a single copy transgene insertion of P*snt-1* promoter driving CaV1-HALO in neurons and stained with HTL-JF646. Veli / LIN7 was tagged with SNAP and stained with STL-JF549cp, and was expressed in acetylcholine neurons using the *unc-129* promotor as an extrachromosomal array. scale bar = 1um. Localization microscopy images of dorsal nerve cord. Dense projections are marked by RIMBP-SkylanS.

(D) Single synapse analysis of Veli / LIN7, CaV1, RIMBP. Dense projections are marked by RIMBP-SkylanS. In the CaV1(Δns) background, CaV1 was rescued in neurons using a single copy transgene insertion of the P*snt-1* promoter driving CaV1-HALO, and stained with HTL-JF646. Veli/ LIN7 was expressed in acetylcholine neurons using the P*unc-129* promotor as an extrachromosomal array, and tagged with SNAP and stained with STL-JF549cp and. Scale bar = 250nm.

(E-G) Cumulative distribution plot of P*snt-1*:CaV1-HALO to RIMBP-SkylanS center, and Veli / LIN7 tagged with SNAP to RIMBP-SkylanS center measured from synaptic regions. n=24 synapses, N=5 animals. Data available as Source Data 5

830 **Figure 6. CaV1 and RyR are adjacent.**
831 (A) CaV1 and RyR are adjacent along the dorsal nerve cord, lateral to the dense projection. Animals
832 and HTL-JF646. Scale bar = 1um. CaV1-SNAP is labelled with STL-JF549pa, RyR-HALO is labelled
833 with HTL-JF646, and dense projections are labeled by ELKS-Skylan-S.
834 (B) RyR and CaV1 colocalize within synapses. Labelling as in 'A'. Scale bar = 250nm.
835 (C) Distances from CaV1-SNAP localizations to center of ELKS-Skylan-S cluster versus ELKS
836 localizations to ELKS center. Distances from RyR-HALO localizations to center of ELKS-Skylan-S
837 cluster versus ELKS localizations to ELKS center. Distances from CaV1-SNAP localizations to the
838 center of the RyR-HALO cluster versus RyR-HALO localizations to the RyR center. N=5 animals,
839 n=25 synapses.
840 (D) RyR and CaV1 are adjacent. Left, nearest neighbor analysis was performed on CaV1-SNAP
841 localizations to find the nearest RyR-HALO localization. Right, nearest neighbor distances from RyR-
842 HALO to CaV1-SNAP were calculated. n=5 animals, 25 synapses.
843 Data available as Source Data 5

844

845 **Figure 7. UNC-13 isoforms colocalize with CaV2 and CaV1 calcium channels.**
846 Localization microscopy identifies CaV1 and CaV2 associated with 'UNC13all', which labels a C-
847 terminal site common to all UNC-13 isoforms.
848 (A) UNC-13all colocalizes with CaV1 and CaV2 along the dorsal nerve cord. Proteins are labelled
849 with CaV2-HALO stained with HTL-JF646, CaV1-SNAP stained with STL-JF549, and UNC13all-
850 Skylan-S.
851 (B) UNC-13all colocalizes with CaV1 and CaV2 within synapses. Staining as in 'A'.
852 (C) Left, distances from CaV1-SNAP localizations to the center of the CaV2-HALO cluster, and
853 CaV2-HALO localizations to the center of the CaV2-HALO cluster. Middle, distances from UNC13all-
854 Skylan-S localizations to the center of the CaV2-HALO cluster. Right, distances from UNC13all-
855 Skylan-S localizations to the center of the CaV1-SNAP cluster, n=5 animals, 25 synapses.
856 (D) Left, nearest-neighbor distances between UNC13all and CaV1 and CaV2 localizations. Right,
857 nearest neighbor analysis between UNC13all-SkylanS and CaV2-HALO or CaV1-SNAP measured
858 from synaptic regions, n=5 animals, 25 synapses. Data available as Source Data 5
859

860 **Figure 8. UNC-13S is associated with CaV1 calcium channels.**
861 Localization microscopy identifies CaV1 associated with UNC13s which labels a n-terminal site
862 common to a short isoform.
863 (A) UNC-13S localizes with CaV1 along the dorsal cord, but not with CaV2. The endogenous protein
864 tags CaV2-HALO was stained with HTL-JF646 , CaV1-SNAP with STL-JF549, and imaged with
865 Skylan-S-UNC13S using single-molecule localization microscopy.
866 (B) UNC-13S localizes with CaV1 within synapses. Strain was labelled as in 'A'.
867 (C) Left, distances from CaV1-SNAP localizations to the center of the CaV2-HALO cluster compared
868 to CaV2-HALO localizations to their own center. Middle, distances from Skylan-UNC13S
869 localizations to the center of the CaV2-HALO cluster. Right, distances from Skylan-UNC13S
870 localizations to the center of the CaV1-SNAP cluster. N=5 animals, 25 synapses
871 (D) Nearest-neighbor distances of CaV1-SNAP to Skylan-UNC13S localizations. Nearest neighbor
872 analysis of Skylan-UNC13S to CaV1-SNAP measured from synaptic regions. N=5 animals, 25
873 synapses. Data available as Source Data 5

874 **Figure 9. Two independent release sites for synaptic vesicles.**
875 Voltage-gated calcium channels localize to two distinct zones at the neuromuscular synapse of *C.*
876 *elegans*. The CaV2 channel localizes to the dense projection along with ELKS, RIMBP, Neurexin,
877 Liprin-alpha, SYDE, MAGI1, alpha-Catulin and the SNARE priming protein UNC-13L. CaV2 is
878 required to fuse synaptic vesicles are docked directly adjacent to the dense projection. The second
879 channel CaV1 is at a lateral site centered 300nm from the dense projection but can span hundreds
880 of nanometers. CaV1 requires coupling to RyR to synaptic vesicles at the lateral site. These near
881 and far pools utilize specific release machinery. Most UNC-13all localizes to the dense projection.
882 However, some UNC-13 localizes with CaV1 at the lateral site. Isoform specific tagging shows UNC-
883 13S localized with lateral site.

884 **References**

885 Ackermann, F., Waites, C. L., & Garner, C. C. (2015). Presynaptic active zones in invertebrates
886 and vertebrates. *EMBO Reports*, *16*(8). https://doi.org/10.15252/embr.201540434
887 Augustin, I., Rosenmund, C., Südhof, T. C., & Brose, N. (1999). Munc13-1 is essential for fusion
888 competence of glutamatergic synaptic vesicles. *Nature*, *400*(6743), 457–461.
889 https://doi.org/10.1038/22768
890 Basu, J., Betz, A., Brose, N., & Rosenmund, C. (2007). Munc13-1 C1 Domain Activation Lowers
891 the Energy Barrier for Synaptic Vesicle Fusion. *The Journal of Neuroscience*, *27*(5), 1200.
892 https://doi.org/10.1523/JNEUROSCI.4908-06.2007
893 Betz, A., Thakur, P., Junge, H. J., Ashery, U., Rhee, J.-S., Scheuss, V., … Brose, N. (2001).
894 Functional Interaction of the Active Zone Proteins Munc13-1 and RIM1 in Synaptic Vesicle
895 Priming. *Neuron*, *30*(1), 183–196. https://doi.org/https://doi.org/10.1016/S0896-
896 6273(01)00272-0
897 Blaustein, M. P. (1988). Calcium transport and buffering in neurons. *Trends in Neurosciences*,
898 *11*(10), 438–443. https://doi.org/https://doi.org/10.1016/0166-2236(88)90195-6
899 Böhme, M. A., Beis, C., Reddy-Alla, S., Reynolds, E., Mampell, M. M., Grasskamp, A. T., …
900 Sigrist, S. J. (2016). Active zone scaffolds differentially accumulate Unc13 isoforms to tune
901 Ca2+ channel–vesicle coupling. *Nature Neuroscience*, *19*(10), 1311–1320.
902 https://doi.org/10.1038/nn.4364
903 Bouchard, R., Pattarini, R., & Geiger, J. D. (2003). Presence and functional significance of
904 presynaptic ryanodine receptors. *Progress in Neurobiology*, *69*(6), 391–418.
905 https://doi.org/https://doi.org/10.1016/S0301-0082(03)00053-4
906 Butz, S., Okamoto, M., & Südhof, T. C. (1998). A Tripartite Protein Complex with the Potential to
907 Couple Synaptic Vesicle Exocytosis to Cell Adhesion in Brain. *Cell*, *94*(6), 773–782.
908 https://doi.org/https://doi.org/10.1016/S0092-8674(00)81736-5
909 Cardona, A., Saalfeld, S., Schindelin, J., Arganda-Carreras, I., Preibisch, S., Longair, M., …
910 Douglas, R. J. (2012). TrakEM2 Software for Neural Circuit Reconstruction. *PLoS ONE*,
911 *7*(6), e38011. https://doi.org/10.1371/journal.pone.0038011
912 Catterall, W. A., Perez-Reyes, E., Snutch, T. P., & Striessnig, J. (2005). International Union of
913 Pharmacology. XLVIII. Nomenclature and Structure-Function Relationships of Voltage-
914 Gated Calcium Channels. *Pharmacological Reviews*, *57*(4), 411.
915 https://doi.org/10.1124/pr.57.4.5
916 Chen, B., Liu, P., Hujber, E. J., Li, Y., Jorgensen, E. M., & Wang, Z.-W. (2017). AIP limits
917 neurotransmitter release by inhibiting calcium bursts from the ryanodine receptor. *Nature*
918 *Communications*, *8*(1), 1380. https://doi.org/10.1038/s41467-017-01704-z
919 Courtney, N. A., Briguglio, J. S., Bradberry, M. M., Greer, C., & Chapman, E. R. (2018).

Excitatory and Inhibitory Neurons Utilize Different Ca(2+) Sensors and Sources to Regulate Spontaneous Release. *Neuron*, *98*(5), 977-991.e5. https://doi.org/10.1016/j.neuron.2018.04.022

del Castillo, J., & Katz, B. (1954). Quantal components of the end-plate potential. *The Journal of Physiology*, *124*(3), 560.

Dickinson, D. J., Ward, J. D., Reiner, D. J., & Goldstein, B. (2013). Engineering the Caenorhabditis elegans genome using Cas9-triggered homologous recombination. *Nature Methods*, *10*(10), 1028–1034. https://doi.org/10.1038/nmeth.2641

Dittman, J. S. (2019). Unc13: a multifunctional synaptic marvel. *Current Opinion in Neurobiology*, *57*, 17–25. https://doi.org/https://doi.org/10.1016/j.conb.2018.12.011

Dittman, J. S., & Ryan, T. A. (2019). The control of release probability at nerve terminals. *Nature Reviews Neuroscience*, *20*(3), 177–186. https://doi.org/10.1038/s41583-018-0111-3

Dolphin, A. C. (2021). Functions of Presynaptic Voltage-gated Calcium Channels. *Function*, *2*(1), zqaa027. https://doi.org/10.1093/function/zqaa027

Dolphin, A. C., & Lee, A. (2020). Presynaptic calcium channels: specialized control of synaptic neurotransmitter release. *Nature Reviews Neuroscience*, *21*(4), 213–229. https://doi.org/10.1038/s41583-020-0278-2

Eggermann, E., Bucurenciu, I., Goswami, S. P., & Jonas, P. (2012). Nanodomain coupling between Ca2+ channels and sensors of exocytosis at fast mammalian synapses. *Nature Reviews Neuroscience*, *13*(1), 7–21. https://doi.org/10.1038/nrn3125

Eguchi, K., Montanaro, J., le Monnier, E., & Shigemoto, R. (2022). The Number and Distinct Clustering Patterns of Voltage-Gated Calcium Channels in Nerve Terminals. *Frontiers in Neuroanatomy*, *16*. Retrieved from https://www.frontiersin.org/article/10.3389/fnana.2022.846615

Encell, L. P. (2013). Development of a Dehalogenase-Based Protein Fusion Tag Capable of Rapid, Selective and Covalent Attachment to Customizable Ligands. *Current Chemical Genomics*, *6*(1), 55–71. https://doi.org/10.2174/1875397301206010055

Fedchyshyn, M. J., & Wang, L.-Y. (2005). Developmental Transformation of the Release Modality at the Calyx of Held Synapse. *The Journal of Neuroscience*, *25*(16), 4131. https://doi.org/10.1523/JNEUROSCI.0350-05.2005

Frøkjær-Jensen, C., Davis, M. W., Sarov, M., Taylor, J., Flibotte, S., LaBella, M., … Jorgensen, E. M. (2014). Random and targeted transgene insertion in Caenorhabditis elegans using a modified Mos1 transposon. *Nature Methods*, *11*(5), 529–534. https://doi.org/10.1038/nmeth.2889

Frøkjær-Jensen, C., Wayne Davis, M., Hopkins, C. E., Newman, B. J., Thummel, J. M., Olesen, S.-P., … Jorgensen, E. M. (2008). Single-copy insertion of transgenes in Caenorhabditis

elegans. *Nature Genetics*, *40*(11), 1375–1383. https://doi.org/10.1038/ng.248

Galante, M., & Marty, A. (2003). Presynaptic Ryanodine-Sensitive Calcium Stores Contribute to Evoked Neurotransmitter Release at the Basket Cell-Purkinje Cell Synapse. *The Journal of Neuroscience*, *23*(35), 11229. https://doi.org/10.1523/JNEUROSCI.23-35-11229.2003

Geppert, M., Goda, Y., Hammer, R. E., Li, C., Rosahl, T. W., Stevens, C. F., & Südhof, T. C. (1994). Synaptotagmin I: A major Ca2+ sensor for transmitter release at a central synapse. *Cell*, *79*(4), 717–727. https://doi.org/https://doi.org/10.1016/0092-8674(94)90556-8

Goswami, S. P., Bucurenciu, I., & Jonas, P. (2012). Miniature IPSCs in Hippocampal Granule Cells Are Triggered by Voltage-Gated Ca²⁺ Channels via Microdomain Coupling. *The Journal of Neuroscience*, *32*(41), 14294. https://doi.org/10.1523/JNEUROSCI.6104-11.2012

Gracheva, E. O., Hadwiger, G., Nonet, M. L., & Richmond, J. E. (2008). Direct interactions between C. elegans RAB-3 and Rim provide a mechanism to target vesicles to the presynaptic density. *Neuroscience Letters*, *444*(2), 137–142. https://doi.org/https://doi.org/10.1016/j.neulet.2008.08.026

Grimm, J. B., Brown, T. A., English, B. P., Lionnet, T., & Lavis, L. D. (2017). *Synthesis of Janelia Fluor HaloTag and SNAP-Tag Ligands and Their Use in Cellular Imaging Experiments*. https://doi.org/10.1007/978-1-4939-7265-4_15

Grimm, J. B., English, B. P., Chen, J., Slaughter, J. P., Zhang, Z., Revyakin, A., … Lavis, L. D. (2015). A general method to improve fluorophores for live-cell and single-molecule microscopy. *Nature Methods*, *12*(3), 244–250. https://doi.org/10.1038/nmeth.3256

Guzikowski, N. J., & Kavalali, E. T. (2021). Nano-Organization at the Synapse: Segregation of Distinct Forms of Neurotransmission. *Frontiers in Synaptic Neuroscience*, *13*, 796498. https://doi.org/10.3389/fnsyn.2021.796498

Hammarlund, M., Palfreyman, M. T., Watanabe, S., Olsen, S., & Jorgensen, E. M. (2007). Open Syntaxin Docks Synaptic Vesicles. *PLOS Biology*, *5*(8), e198-. Retrieved from https://doi.org/10.1371/journal.pbio.0050198

Hell, J. W., Westenbroek, R. E., Breeze, L. J., Wang, K. K., Chavkin, C., & Catterall, W. A. (1996). N-methyl-D-aspartate receptor-induced proteolytic conversion of postsynaptic class C L-type calcium channels in hippocampal neurons. *Proceedings of the National Academy of Sciences*, *93*(8), 3362–3367. https://doi.org/10.1073/pnas.93.8.3362

Hell, J. W., Westenbroek, R. E., Warner, C., Ahlijanian, M. K., Prystay, W., Gilbert, M. M., … Catterall, W. A. (1993). Identification and differential subcellular localization of the neuronal class C and class D L-type calcium channel alpha 1 subunits. *Journal of Cell Biology*, *123*(4), 949–962. https://doi.org/10.1083/jcb.123.4.949

Hu, Z., Tong, X.-J., & Kaplan, J. M. (2013). UNC-13L, UNC-13S, and Tomosyn form a protein

992 code for fast and slow neurotransmitter release in Caenorhabditis elegans. *ELife*, *2*,
993 e00967. https://doi.org/10.7554/eLife.00967
994 Imig, C., Min, S.-W., Krinner, S., Arancillo, M., Rosenmund, C., Südhof, T. C., … Cooper, B. H.
995 (2014). The Morphological and Molecular Nature of Synaptic Vesicle Priming at
996 Presynaptic Active Zones. *Neuron*, *84*(2), 416–431.
997 https://doi.org/https://doi.org/10.1016/j.neuron.2014.10.009
998 J.G. White, E. Southgate, J.N. Thomson, & S. Brenner. (1986). The structure of the nervous
999 system of the nematode *Caenorhabditis elegans*. *Philosophical Transactions of the Royal*
1000 *Society of London. B, Biological Sciences*, *314*(1165), 1–340.
1001 https://doi.org/10.1098/rstb.1986.0056
1002 Juette, M. F., Gould, T. J., Lessard, M. D., Mlodzianoski, M. J., Nagpure, B. S., Bennett, B. T.,
1003 … Bewersdorf, J. (2008). Three-dimensional sub–100 nm resolution fluorescence
1004 microscopy of thick samples. *Nature Methods*, *5*(6), 527–529.
1005 https://doi.org/10.1038/nmeth.1211
1006 Katz, E., Ferro, P. A., Weisz, G., & Uchitel, O. D. (1996). Calcium channels involved in synaptic
1007 transmission at the mature and regenerating mouse neuromuscular junction. *The Journal*
1008 *of Physiology*, *497*(3), 687–697. https://doi.org/10.1113/jphysiol.1996.sp021800
1009 Kawabe, H., Mitkovski, M., Kaeser, P. S., Hirrlinger, J., Opazo, F., Nestvogel, D., … Brose, N.
1010 (2017). ELKS1 localizes the synaptic vesicle priming protein bMunc13-2 to a specific
1011 subset of active zones. *The Journal of Cell Biology*, *216*(4), 1143–1161.
1012 https://doi.org/10.1083/jcb.201606086
1013 Kim, S., Yun, H.-M., Baik, J.-H., Chung, K. C., Nah, S.-Y., & Rhim, H. (2007). Functional
1014 Interaction of Neuronal Cav1.3 L-type Calcium Channel with Ryanodine Receptor Type 2 in
1015 the Rat Hippocampus. *Journal of Biological Chemistry*, *282*(45), 32877–32889.
1016 https://doi.org/10.1074/jbc.M701418200
1017 Kurshan, P. T., Merrill, S. A., Dong, Y., Ding, C., Hammarlund, M., Bai, J., … Shen, K. (2018).
1018 γ-Neurexin and Frizzled Mediate Parallel Synapse Assembly Pathways
1019 Antagonized by Receptor Endocytosis. *Neuron*, *100*(1), 150-166.e4.
1020 https://doi.org/10.1016/j.neuron.2018.09.007
1021 Kusick, G. F., Chin, M., Raychaudhuri, S., Lippmann, K., Adula, K. P., Hujber, E. J., …
1022 Watanabe, S. (2020). Synaptic vesicles transiently dock to refill release sites. *Nature*
1023 *Neuroscience*, *23*(11), 1329–1338. https://doi.org/10.1038/s41593-020-00716-1
1024 Kwok, T. C. Y., Ricker, N., Fraser, R., Chan, A. W., Burns, A., Stanley, E. F., … Roy, P. J.
1025 (2006). A small-molecule screen in C. elegans yields a new calcium channel antagonist.
1026 *Nature*, *441*(7089), 91–95. https://doi.org/10.1038/nature04657
1027 Lai, Y., Choi, U. B., Leitz, J., Rhee, H. J., Lee, C., Altas, B., … Brunger, A. T. (2017). Molecular

Mechanisms of Synaptic Vesicle Priming by Munc13 and Munc18. *Neuron*, *95*(3), 591-607.e10. https://doi.org/https://doi.org/10.1016/j.neuron.2017.07.004

Lainé, V., Ségor, J. R., Zhan, H., Bessereau, J.-L., & Jospin, M. (2014). Hyperactivation of L-type voltage-gated Ca2+ channels in Caenorhabditis elegans striated muscle can result from point mutations in the IS6 or the IIIS4 segment of the α1 subunit. *Journal of Experimental Biology*, *217*(21), 3805–3814. https://doi.org/10.1242/jeb.106732

Lee, R. Y., Lobel, L., Hengartner, M., Horvitz, H. R., & Avery, L. (1997). Mutations in the alpha1 subunit of an L-type voltage-activated Ca2+ channel cause myotonia in Caenorhabditis elegans. *The EMBO Journal*, *16*(20), 6066–6076. https://doi.org/10.1093/emboj/16.20.6066

Littleton, J. T., Stern, M., Schulze, K., Perin, M., & Bellen, H. J. (1993). Mutational analysis of Drosophila synaptotagmin demonstrates its essential role in Ca2+-activated neurotransmitter release. *Cell*, *74*(6), 1125–1134. https://doi.org/https://doi.org/10.1016/0092-8674(93)90733-7

Liu, H., Li, L., Nedelcu, D., Hall, Q., Zhou, L., Wang, W., … Hu, Z. (2019). Heterodimerization of UNC-13/RIM regulates synaptic vesicle release probability but not priming in C. elegans. *ELife*, *8*, e40585. https://doi.org/10.7554/eLife.40585

Liu, H., Li, L., Wang, W., Gong, J., Yang, X., & Hu, Z. (2018). Spontaneous Vesicle Fusion Is Differentially Regulated at Cholinergic and GABAergic Synapses. *Cell Reports*, *22*(9), 2334–2345. https://doi.org/https://doi.org/10.1016/j.celrep.2018.02.023

Liu, P., Ge, Q., Chen, B., Salkoff, L., Kotlikoff, M. I., & Wang, Z.-W. (2011). Genetic dissection of ion currents underlying all-or-none action potentials in C. elegans body-wall muscle cells. *The Journal of Physiology*, *589*(1), 101–117. https://doi.org/10.1113/jphysiol.2010.200683

Liu, Ping, Chen, B., Mailler, R., & Wang, Z.-W. (2017). Antidromic-rectifying gap junctions amplify chemical transmission at functionally mixed electrical-chemical synapses. *Nature Communications*, *8*(1), 14818. https://doi.org/10.1038/ncomms14818

Liu, Ping, Chen, B., & Wang, Z.-W. (2014). SLO-2 potassium channel is an important regulator of neurotransmitter release in Caenorhabditis elegans. *Nature Communications*, *5*(1), 5155. https://doi.org/10.1038/ncomms6155

Liu, Q., Chen, B., Yankova, M., Morest, D. K., Maryon, E., Hand, A. R., … Wang, Z.-W. (2005). Presynaptic ryanodine receptors are required for normal quantal size at the Caenorhabditis elegans neuromuscular junction. *The Journal of Neuroscience : The Official Journal of the Society for Neuroscience*, *25*(29), 6745–6754. https://doi.org/10.1523/JNEUROSCI.1730-05.2005

Liu, Q., Hollopeter, G., & Jorgensen, E. M. (2009). Graded synaptic transmission at the Caenorhabditis elegans neuromuscular junction. *Proceedings of the National Academy of Sciences*, *106*(26), 10823. https://doi.org/10.1073/pnas.0903570106

Liu, Q., Kidd, P. B., Dobosiewicz, M., & Bargmann, C. I. (2018). C. elegans AWA Olfactory Neurons Fire Calcium-Mediated All-or-None Action Potentials. *Cell*, *175*(1), 57-70.e17. https://doi.org/https://doi.org/10.1016/j.cell.2018.08.018

Llano, I., González, J., Caputo, C., Lai, F. A., Blayney, L. M., Tan, Y. P., & Marty, A. (2000). Presynaptic calcium stores underlie large-amplitude miniature IPSCs and spontaneous calcium transients. *Nature Neuroscience*, *3*(12), 1256–1265. https://doi.org/10.1038/81781

Los, G. v, Encell, L. P., McDougall, M. G., Hartzell, D. D., Karassina, N., Zimprich, C., … Wood, K. v. (2008). HaloTag: A Novel Protein Labeling Technology for Cell Imaging and Protein Analysis. *ACS Chemical Biology*, *3*(6), 373–382. https://doi.org/10.1021/cb800025k

Lu, J., Machius, M., Dulubova, I., Dai, H., Südhof, T. C., Tomchick, D. R., & Rizo, J. (2006). Structural Basis for a Munc13–1 Homodimer to Munc13–1/RIM Heterodimer Switch. *PLOS Biology*, *4*(7), e192-. Retrieved from https://doi.org/10.1371/journal.pbio.0040192

Maduro, M., & Pilgrim, D. (1995). Identification and cloning of unc-119, a gene expressed in the Caenorhabditis elegans nervous system. *Genetics*, *141*(3), 977–988. https://doi.org/10.1093/genetics/141.3.977

Marques, F., Thapliyal, S., Javer, A., Shrestha, P., Brown, A. E. X., & Glauser, D. A. (2020). Tissue-specific isoforms of the single C. elegans Ryanodine receptor gene unc-68 control specific functions. *PLOS Genetics*, *16*(10), e1009102. https://doi.org/10.1371/journal.pgen.1009102

McRory, J. E., Hamid, J., Doering, C. J., Garcia, E., Parker, R., Hamming, K., … Snutch, T. P. (2004). The CACNA1F Gene Encodes an L-Type Calcium Channel with Unique Biophysical Properties and Tissue Distribution. *The Journal of Neuroscience*, *24*(7), 1707. https://doi.org/10.1523/JNEUROSCI.4846-03.2004

Michelassi, F., Liu, H., Hu, Z., & Dittman, J. S. (2017). A C1-C2 Module in Munc13 Inhibits Calcium-Dependent Neurotransmitter Release. *Neuron*, *95*(3), 577-590.e5. https://doi.org/https://doi.org/10.1016/j.neuron.2017.07.015

Mlodzianoski, M. J., Juette, M. F., Beane, G. L., & Bewersdorf, J. (2009). Experimental characterization of 3D localization techniques for particle-tracking and super-resolution microscopy. *Opt. Express*, *17*(10), 8264–8277. https://doi.org/10.1364/OE.17.008264

Mollwitz, B., Brunk, E., Schmitt, S., Pojer, F., Bannwarth, M., Schiltz, M., … Johnsson, K. (2012). Directed Evolution of the Suicide Protein O^6-Alkylguanine-DNA Alkyltransferase for Increased Reactivity Results in an Alkylated Protein with Exceptional Stability. *Biochemistry*, *51*(5), 986–994. https://doi.org/10.1021/bi2016537

Nakamura, Y., Harada, H., Kamasawa, N., Matsui, K., Rothman, J. S., Shigemoto, R., … Takahashi, T. (2015). Nanoscale Distribution of Presynaptic Ca2+ Channels and Its Impact on Vesicular Release during Development. *Neuron*, *85*(1), 145–158.

https://doi.org/https://doi.org/10.1016/j.neuron.2014.11.019

Nanou, E., & Catterall, W. A. (2018). Calcium Channels, Synaptic Plasticity, and Neuropsychiatric Disease. *Neuron*, *98*(3), 466–481. https://doi.org/https://doi.org/10.1016/j.neuron.2018.03.017

Naranjo, D., Wen, H., & Brehm, P. (2015). Zebrafish CaV2.1 Calcium Channels Are Tailored for Fast Synchronous Neuromuscular Transmission. *Biophysical Journal*, *108*(3), 578–584. https://doi.org/https://doi.org/10.1016/j.bpj.2014.11.3484

Neher, E., & Brose, N. (2018). Dynamically Primed Synaptic Vesicle States: Key to Understand Synaptic Short-Term Plasticity. *Neuron*, *100*(6), 1283–1291. https://doi.org/https://doi.org/10.1016/j.neuron.2018.11.024

Nowycky, M. C., Fox, A. P., & Tsien, R. W. (1985). Three types of neuronal calcium channel with different calcium agonist sensitivity. *Nature*, *316*(6027), 440–443. https://doi.org/10.1038/316440a0

Özçete, Ö. D., & Moser, T. (2021). A sensory cell diversifies its output by varying Ca2+ influx-release coupling among active zones. *The EMBO Journal*, *40*(5), e106010. https://doi.org/https://doi.org/10.15252/embj.2020106010

Piggott, C. A., & Jin, Y. (2021). Junctophilins: Key Membrane Tethers in Muscles and Neurons. *Frontiers in Molecular Neuroscience*, *14*, 141. Retrieved from https://www.frontiersin.org/article/10.3389/fnmol.2021.709390

Platzer, J., Engel, J., Schrott-Fischer, A., Stephan, K., Bova, S., Chen, H., … Striessnig, J. (2000). Congenital Deafness and Sinoatrial Node Dysfunction in Mice Lacking Class D L-Type Ca2+ Channels. *Cell*, *102*(1), 89–97. https://doi.org/https://doi.org/10.1016/S0092-8674(00)00013-1

Pokala, N., Liu, Q., Gordus, A., & Bargmann, C. I. (2014). Inducible and titratable silencing of Caenorhabditis elegans neurons in vivo with histamine-gated chloride channels. *Proceedings of the National Academy of Sciences*, *111*(7), 2770–2775. https://doi.org/10.1073/pnas.1400615111

Pym, E., Sasidharan, N., Thompson-Peer, K. L., Simon, D. J., Anselmo, A., Sadreyev, R., … Kaplan, J. M. (2017). Shank is a dose-dependent regulator of Cav1 calcium current and CREB target expression. *ELife*, *6*, e18931. https://doi.org/10.7554/eLife.18931

Quade, B., Camacho, M., Zhao, X., Orlando, M., Trimbuch, T., Xu, J., … Rizo, J. (2019). Membrane bridging by Munc13-1 is crucial for neurotransmitter release. *ELife*, *8*, e42806. https://doi.org/10.7554/eLife.42806

Rebola, N., Reva, M., Kirizs, T., Szoboszlay, M., Lőrincz, A., Moneron, G., … DiGregorio, D. A. (2019). Distinct Nanoscale Calcium Channel and Synaptic Vesicle Topographies Contribute to the Diversity of Synaptic Function. *Neuron*, *104*(4), 693-710.e9.

https://doi.org/https://doi.org/10.1016/j.neuron.2019.08.014

Rey, S., Maton, G., Satake, S., Llano, I., Kang, S., Surmeier, D. J., … Collin, T. (2020). Physiological involvement of presynaptic L-type voltage-dependent calcium channels in GABA release of cerebellar molecular layer interneurons. *Journal of Neurochemistry*, *155*(4), 390–402. https://doi.org/10.1111/jnc.15100

Richmond, J E, Weimer, R. M., & Jorgensen, E. M. (2001). An open form of syntaxin bypasses the requirement for UNC-13 in vesicle priming. *Nature*, *412*(6844), 338–341. https://doi.org/10.1038/35085583

Richmond, Janet E, Davis, W. S., & Jorgensen, E. M. (1999). UNC-13 is required for synaptic vesicle fusion in C. elegans. *Nature Neuroscience*, *2*(11), 959–964. https://doi.org/10.1038/14755

Sahu, G., Wazen, R.-M., Colarusso, P., Chen, S. R. W., Zamponi, G. W., & Turner, R. W. (2019). Junctophilin Proteins Tether a Cav1-RyR2-KCa3.1 Tripartite Complex to Regulate Neuronal Excitability. *Cell Reports*, *28*(9), 2427-2442.e6. https://doi.org/https://doi.org/10.1016/j.celrep.2019.07.075

Schneggenburger, R., & Neher, E. (2000). Intracellular calcium dependence of transmitter release rates at a fast central synapse. *Nature*, *406*(6798), 889–893. https://doi.org/10.1038/35022702

Schneider, M. F. (1994). Control of Calcium Release in Functioning Skeletal Muscle Fibers. *Annual Review of Physiology*, *56*(1), 463–484. https://doi.org/10.1146/annurev.ph.56.030194.002335

Schwartz, M. L., & Jorgensen, E. M. (2016). SapTrap, a Toolkit for High-Throughput CRISPR/Cas9 Gene Modification in Caenorhabditis elegans. *Genetics*, *202*(4), 1277–1288. https://doi.org/10.1534/genetics.115.184275

Siksou, L., Varoqueaux, F., Pascual, O., Triller, A., Brose, N., & Marty, S. (2009). A common molecular basis for membrane docking and functional priming of synaptic vesicles. *European Journal of Neuroscience*, *30*(1), 49–56. https://doi.org/https://doi.org/10.1111/j.1460-9568.2009.06811.x

Smith, L. A., Wang, X., Peixoto, A. A., Neumann, E. K., Hall, L. M., & Hall, J. C. (1996). A Drosophila Calcium Channel α1 Subunit Gene Maps to a Genetic Locus Associated with Behavioral and Visual Defects. *The Journal of Neuroscience*, *16*(24), 7868. https://doi.org/10.1523/JNEUROSCI.16-24-07868.1996

Südhof, T. C. (2012). The Presynaptic Active Zone. *Neuron*, *75*(1), 11–25. https://doi.org/https://doi.org/10.1016/j.neuron.2012.06.012

Tong, X.-J., López-Soto, E. J., Li, L., Liu, H., Nedelcu, D., Lipscombe, D., … Kaplan, J. M.

(2017). Retrograde Synaptic Inhibition Is Mediated by α-Neurexin Binding to the α2δ Subunits of N-Type Calcium Channels. *Neuron*, *95*(2), 326-340.e5. https://doi.org/https://doi.org/10.1016/j.neuron.2017.06.018

Topalidou, I., Cattin-Ortolá, J., Pappas, A. L., Cooper, K., Merrihew, G. E., MacCoss, M. J., & Ailion, M. (2016). The EARP Complex and Its Interactor EIPR-1 Are Required for Cargo Sorting to Dense-Core Vesicles. *PLOS Genetics*, *12*(5), e1006074. https://doi.org/10.1371/journal.pgen.1006074

Tsien, R W, Lipscombe, D., Madison, D. v, Bley, K. R., & Fox, A. P. (1988). Multiple types of neuronal calcium channels and their selective modulation. *Trends in Neurosciences*, *11*(10), 431–438. https://doi.org/https://doi.org/10.1016/0166-2236(88)90194-4

Tsien, Richard W, & Tsien, R. Y. (1990). Calcium channels, stores, and oscillations. *Annual Review of Cell Biology*, *6*(1), 715–760.

Urbano, F. J., & Uchitel, O. D. (1999). L-Type calcium channels unmasked by cell-permeant Ca 2+ buffer at mouse motor nerve terminals. *Pfl◆gers Archiv European Journal of Physiology*, *437*(4), 523–528. https://doi.org/10.1007/s004240050813

Vyleta, N. P., & Jonas, P. (2014). Loose Coupling Between Ca $^{2+}$ Channels and Release Sensors at a Plastic Hippocampal Synapse. *Science*, *343*(6171), 665–670. https://doi.org/10.1126/science.1244811

Ward, T., Weber, T., & Chapman, E. (2004). Reconstitution of Ca2+-Regulated Membrane Fusion by Synaptotagmin and SNAREs. *Science*, *304*(5669), 435–438. https://doi.org/10.1126/science.1097196

Watanabe, S., Davis, M. W., Kusick, G. F., Iwasa, J., & Jorgensen, E. M. (2020). SynapsEM: Computer-Assisted Synapse Morphometry. *Frontiers in Synaptic Neuroscience*, *12*. Retrieved from https://www.frontiersin.org/article/10.3389/fnsyn.2020.584549

Watanabe, S., Liu, Q., Davis, M. W., Hollopeter, G., Thomas, N., Jorgensen, N. B., & Jorgensen, E. M. (2013). Ultrafast endocytosis at Caenorhabditis elegans neuromuscular junctions. *ELife*, *2*, e00723. https://doi.org/10.7554/eLife.00723

Weber, A. M., Wong, F. K., Tufford, A. R., Schlichter, L. C., Matveev, V., & Stanley, E. F. (2010). N-type Ca2+ channels carry the largest current: implications for nanodomains and transmitter release. *Nature Neuroscience*, *13*(11), 1348–1350. https://doi.org/10.1038/nn.2657

Weimer, R. M., Gracheva, E. O., Meyrignac, O., Miller, K. G., Richmond, J. E., & Bessereau, J.-L. (2006). UNC-13 and UNC-10/Rim Localize Synaptic Vesicles to Specific Membrane Domains. *The Journal of Neuroscience*, *26*(31), 8040. https://doi.org/10.1523/JNEUROSCI.2350-06.2006

1206 Yang, X., Wang, S., Sheng, Y., Zhang, M., Zou, W., Wu, L., … Ma, C. (2015). Syntaxin opening
1207 by the MUN domain underlies the function of Munc13 in synaptic-vesicle priming. *Nature*
1208 *Structural & Molecular Biology*, *22*(7), 547–554. https://doi.org/10.1038/nsmb.3038
1209 Yu, H., Yuan, C., Westenbroek, R. E., & Catterall, W. A. (2018). The AKAP Cypher/Zasp
1210 contributes to β-adrenergic/PKA stimulation of cardiac CaV1.2 calcium channels. *Journal*
1211 *of General Physiology*, *150*(6), 883–889. https://doi.org/10.1085/jgp.201711818
1212 Zhang, X., Chen, X., Zeng, Z., Zhang, M., Sun, Y., Xi, P., … Xu, P. (2015). Development of a
1213 reversibly switchable fluorescent protein for super-resolution optical fluctuation imaging
1214 (SOFI). *ACS Nano*, *9*(3), 2659–2667. https://doi.org/10.1021/nn5064387
1215 Zheng, W., Feng, G., Ren, D., Eberl, D. F., Hannan, F., Dubald, M., & Hall, L. M. (1995).
1216 Cloning and characterization of a calcium channel alpha 1 subunit from Drosophila
1217 melanogaster with similarity to the rat brain type D isoform. *The Journal of Neuroscience*,
1218 *15*(2), 1132. https://doi.org/10.1523/JNEUROSCI.15-02-01132.1995
1219 Zheng, Y., Brockie, P. J., Mellem, J. E., Madsen, D. M., & Maricq, A. v. (1999). Neuronal Control
1220 of Locomotion in C. elegans Is Modified by a Dominant Mutation in the GLR-1 Ionotropic
1221 Glutamate Receptor. *Neuron*, *24*(2), 347–361.
1222 https://doi.org/https://doi.org/10.1016/S0896-6273(00)80849-1
1223 Zhou, K., Stawicki, T. M., Goncharov, A., & Jin, Y. (2013). Position of UNC-13 in the active zone
1224 regulates synaptic vesicle release probability and release kinetics. *ELife*, *2*, e01180.
1225 https://doi.org/10.7554/eLife.01180
1226

A

viability	+	+	−	+	+	−	+	−	+	+
genotype										
CaV2	+	CaV2(-)	+	+	+	CaV2(-)	CaV2(Δnmj)	CaV2(-)	CaV2(Δnmj)	+
CaV1	+	+	CaV1(-)	CaV1(Δns)	+	+	+	CaV1(Δns)	CaV1(Δns)	CaV1(Δns)
RyR	+	+	+	+	RyR(-)	RyR(-)	RyR(-)	+	+	RyR(-)
strain	N2	AQ130	RW3563	EG9034	CB540	n/a	EG9405	n/a	EG9406	EG8827

B

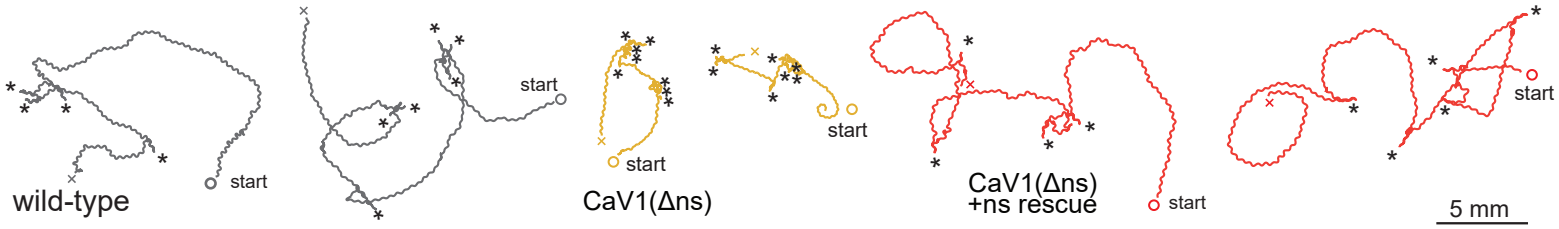

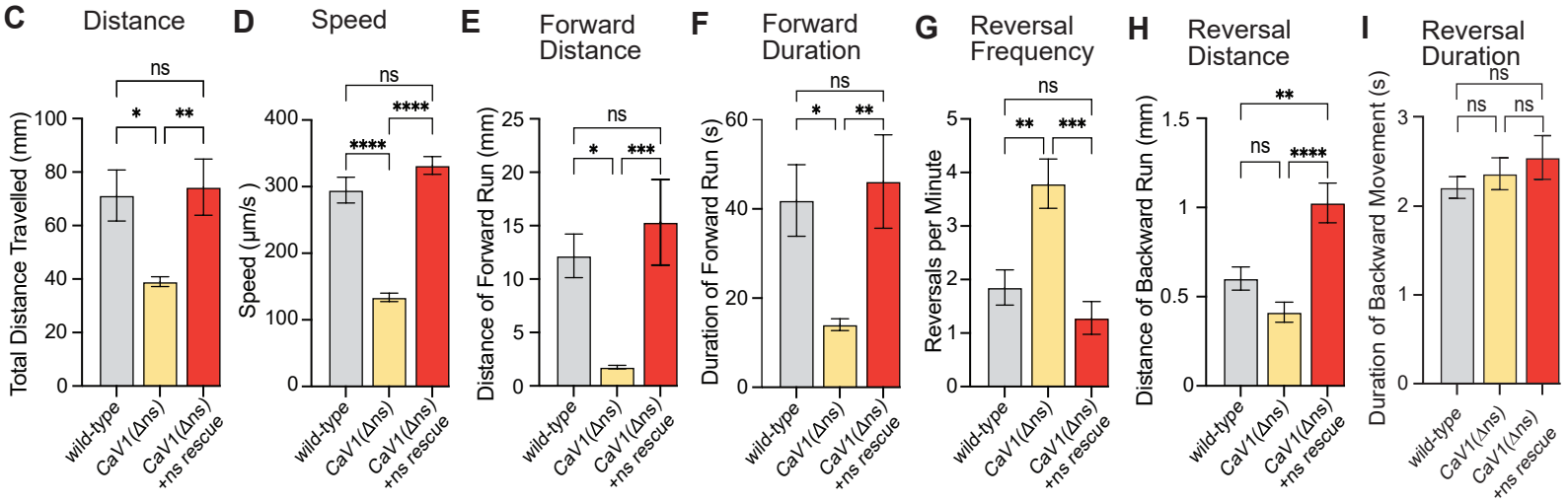

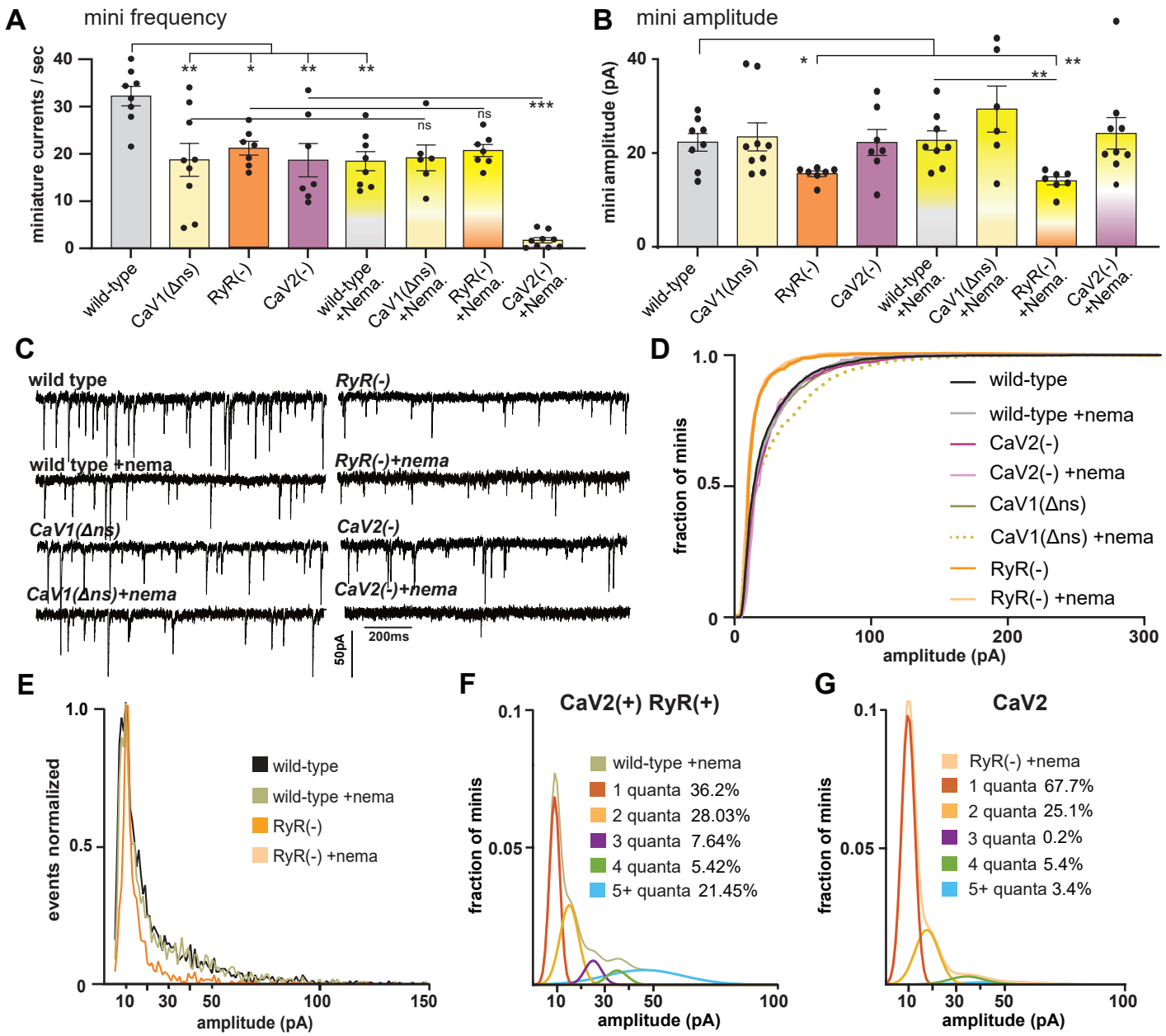
A
mini frequency
miniature currents / sec
40
30
20
10
0
**
*
**
**
***
ns
ns
wild-type
CaV1(Δns)
RyR(-)
CaV2(-)
wild-type +Nema.
CaV1(Δns) +Nema.
RyR(-) +Nema.
CaV2(-) +Nema.
B
mini amplitude
mini amplitude (pA)
40
20
0
*
**
**
wild-type
CaV1(Δns)
RyR(-)
CaV2(-)
wild-type +Nema.
CaV1(Δns) +Nema.
RyR(-) +Nema.
CaV2(-) +Nema.
C
wild type
RyR(-)
wild type +nema
RyR(-)+nema
CaV1(Δns)
CaV2(-)
CaV1(Δns)+nema
CaV2(-)+nema
200ms
50pA
D
fraction of minis
1.0
0.5
0
0
100
200
300
amplitude (pA)
wild-type
wild-type +nema
CaV2(-)
CaV2(-) +nema
CaV1(Δns)
CaV1(Δns) +nema
RyR(-)
RyR(-) +nema
E
events normalized
1.0
0.5
0
10
30
50
100
150
amplitude (pA)
wild-type
wild-type +nema
RyR(-)
RyR(-) +nema
F
CaV2(+) RyR(+)
fraction of minis
0.1
0.05
10
30
50
100
amplitude (pA)
wild-type +nema
1 quanta 36.2%
2 quanta 28.03%
3 quanta 7.64%
4 quanta 5.42%
5+ quanta 21.45%
G
CaV2
fraction of minis
0.1
0.05
10
30
50
100
amplitude (pA)
RyR(-) +nema
1 quanta 67.7%
2 quanta 25.1%
3 quanta 0.2%
4 quanta 5.4%
5+ quanta 3.4%

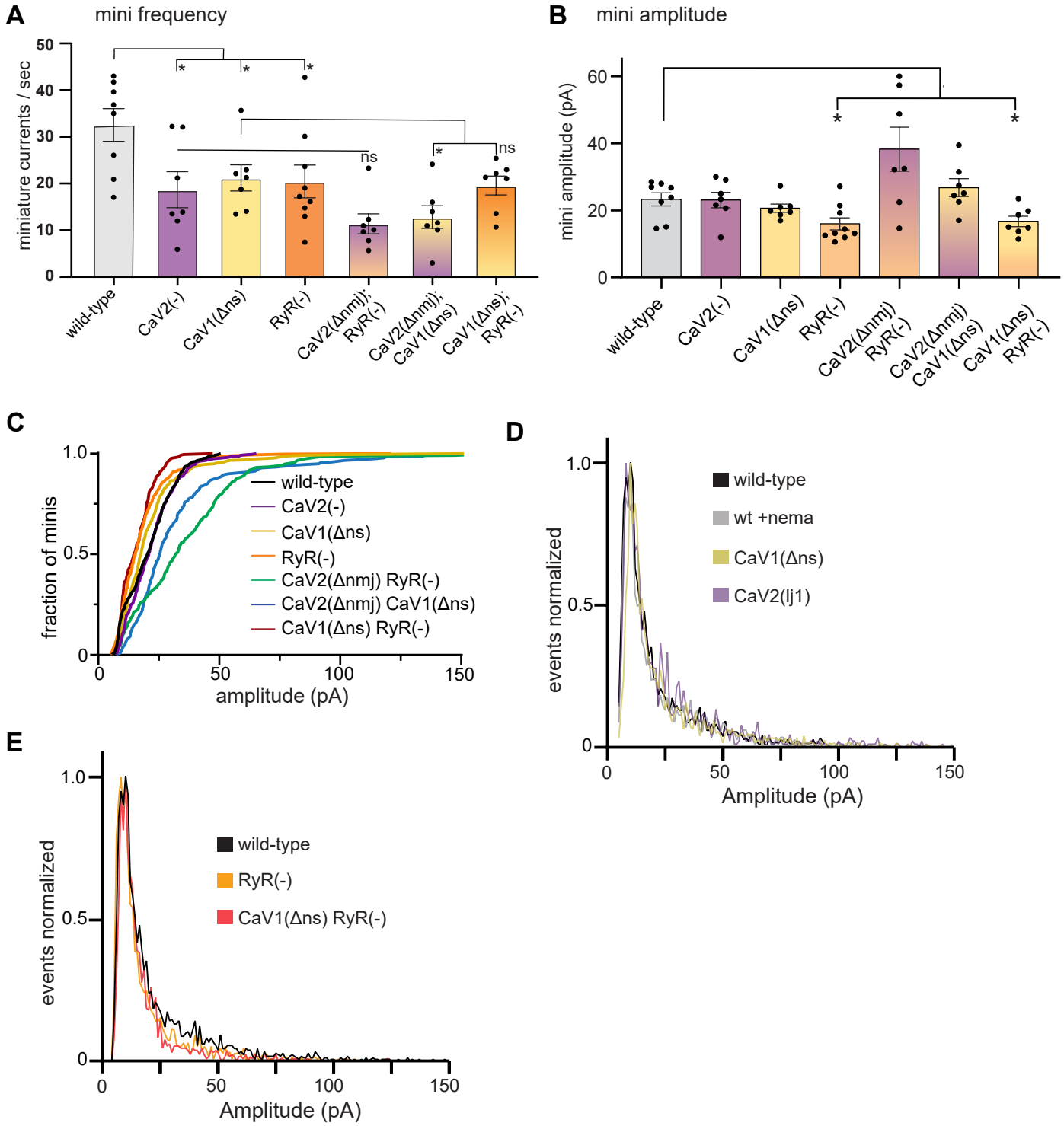
A
mini frequency
miniature currents / sec
50
40
30
20
10
0
*
*
*
ns
*
ns
wild-type
CaV2(-)
CaV1(Δns)
RyR(-)
CaV2(Δnmj); RyR(-)
CaV2(Δnmj); CaV1(Δns)
CaV1(Δns); RyR(-)
B
mini amplitude
mini amplitude (pA)
60
40
20
0
*
*
wild-type
CaV2(-)
CaV1(Δns)
RyR(-)
CaV2(Δnmj) RyR(-)
CaV2(Δnmj) CaV1(Δns)
CaV1(Δns) RyR(-)
C
fraction of minis
1.0
0.5
0
0
50
100
150
amplitude (pA)
wild-type
CaV2(-)
CaV1(Δns)
RyR(-)
CaV2(Δnmj) RyR(-)
CaV2(Δnmj) CaV1(Δns)
CaV1(Δns) RyR(-)
D
events normalized
1.0
0.5
0
0
50
100
150
Amplitude (pA)
wild-type
wt +nema
CaV1(Δns)
CaV2(lj1)
E
events normalized
1.0
0.5
0
0
50
100
150
Amplitude (pA)
wild-type
RyR(-)
CaV1(Δns) RyR(-)

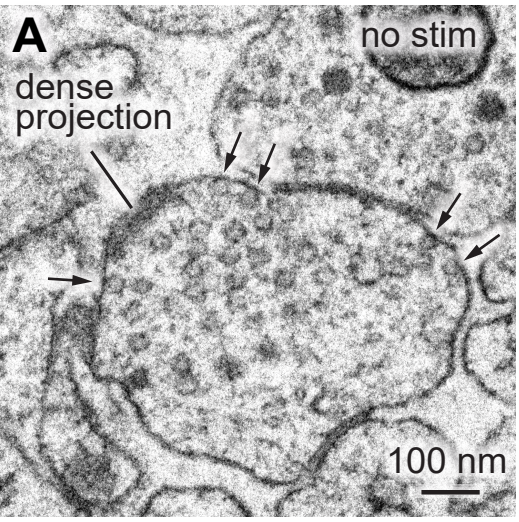
A
no stim
dense projection
100 nm

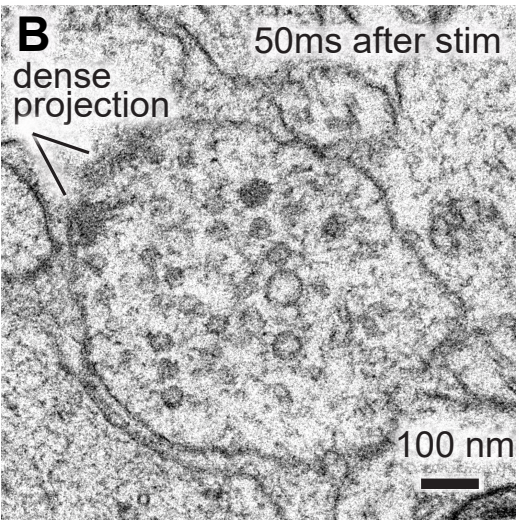
B
50ms after stim
dense projection
100 nm

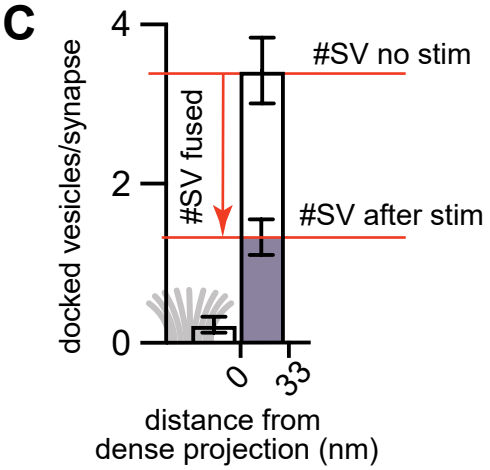
C
docked vesicles/synapse
4
2
0
#SV fused
#SV no stim
#SV after stim
0
33
distance from dense projection (nm)

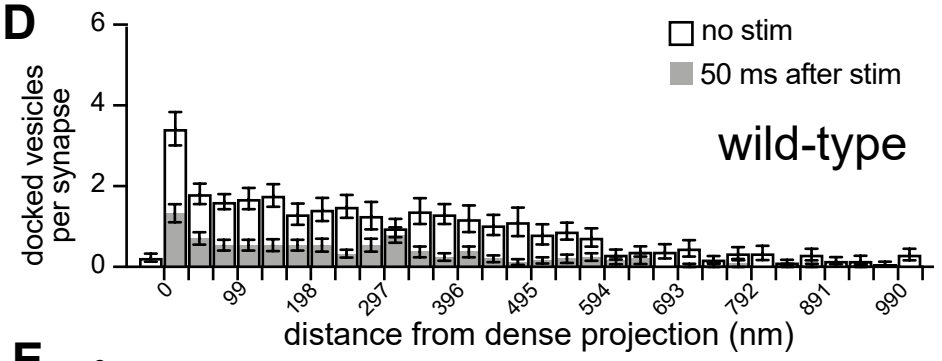
D
no stim
50 ms after stim
wild-type
docked vesicles per synapse
6
4
2
0
0
99
198
297
396
495
594
693
792
891
990
distance from dense projection (nm)

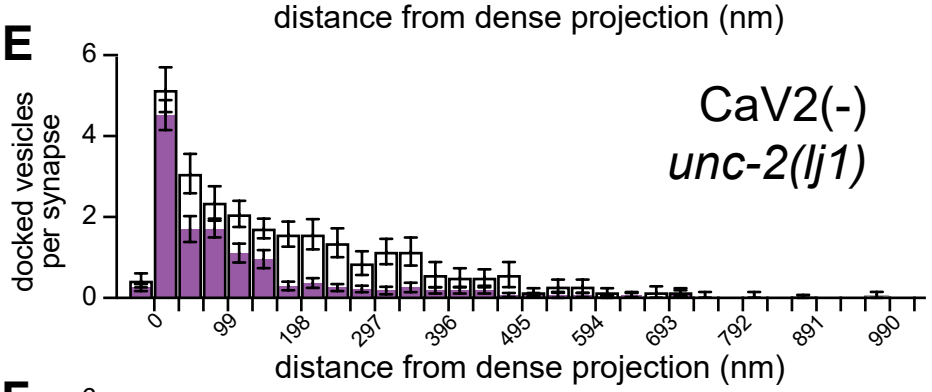
E
CaV2(-)
unc-2(lj1)
docked vesicles per synapse
6
4
2
0
0
99
198
297
396
495
594
693
792
891
990
distance from dense projection (nm)

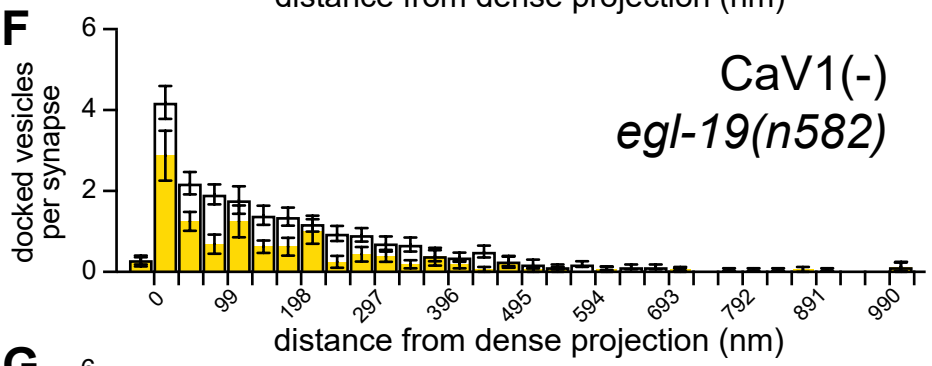
F
CaV1(-)
egl-19(n582)
docked vesicles per synapse
6
4
2
0
0
99
198
297
396
495
594
693
792
891
990
distance from dense projection (nm)

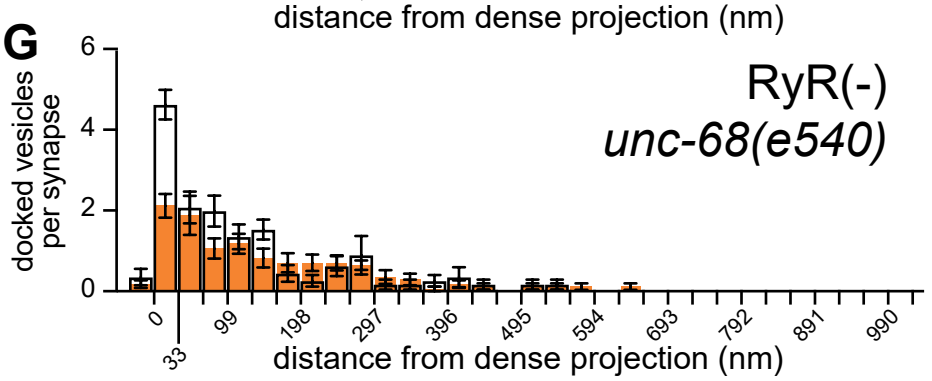
G
RyR(-)
unc-68(e540)
docked vesicles per synapse
6
4
2
0
0
33
99
198
297
396
495
594
693
792
891
990
distance from dense projection (nm)

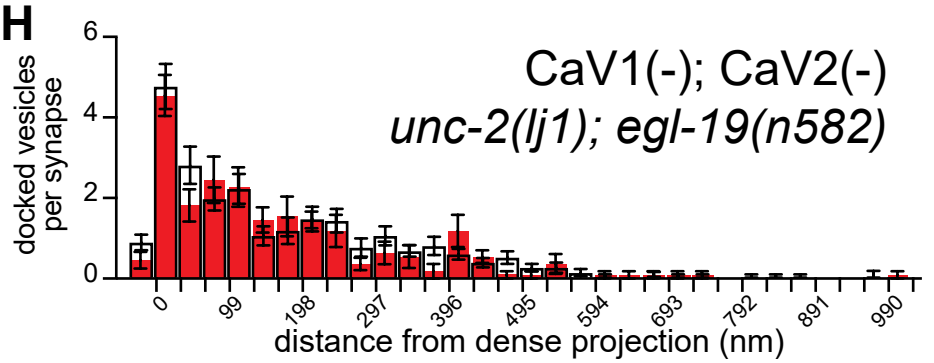
H
CaV1(-); CaV2(-)
unc-2(lj1); egl-19(n582)
docked vesicles per synapse
6
4
2
0
0
99
198
297
396
495
594
693
792
891
990
distance from dense projection (nm)

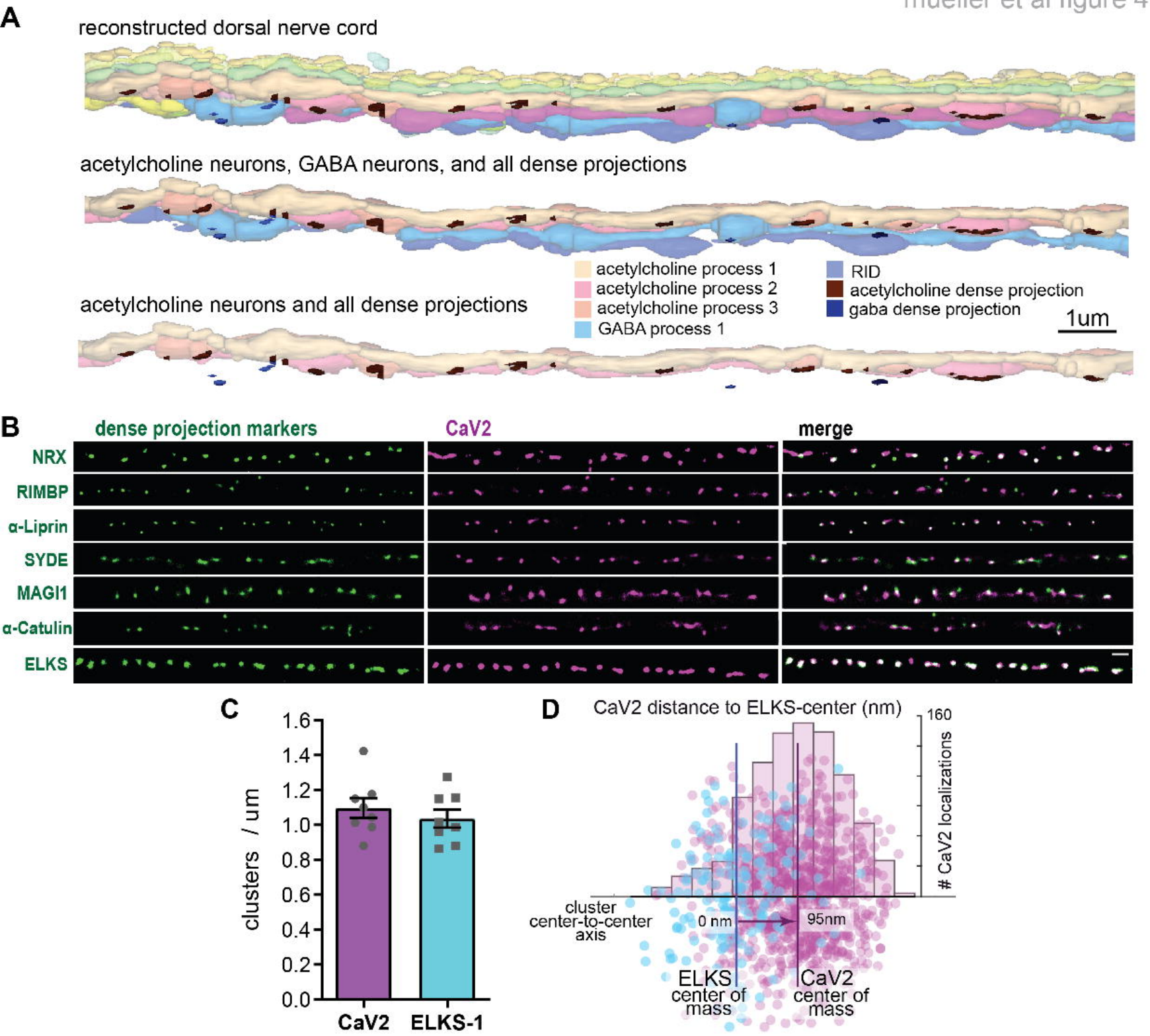
A
reconstructed dorsal nerve cord
acetylcholine neurons, GABA neurons, and all dense projections
acetylcholine neurons and all dense projections
acetylcholine process 1
acetylcholine process 2
acetylcholine process 3
GABA process 1
RID
acetylcholine dense projection
gaba dense projection
1um
B
dense projection markers
CaV2
merge
NRX
RIMBP
α-Liprin
SYDE
MAGI1
α-Catulin
ELKS
C
clusters / um
1.6
1.4
1.2
1.0
0.8
0.6
0.4
0.2
0.0
CaV2
ELKS-1
D
CaV2 distance to ELKS-center (nm)
160
CaV2 localizations
cluster center-to-center axis
0 nm
95nm
ELKS center of mass
CaV2 center of mass

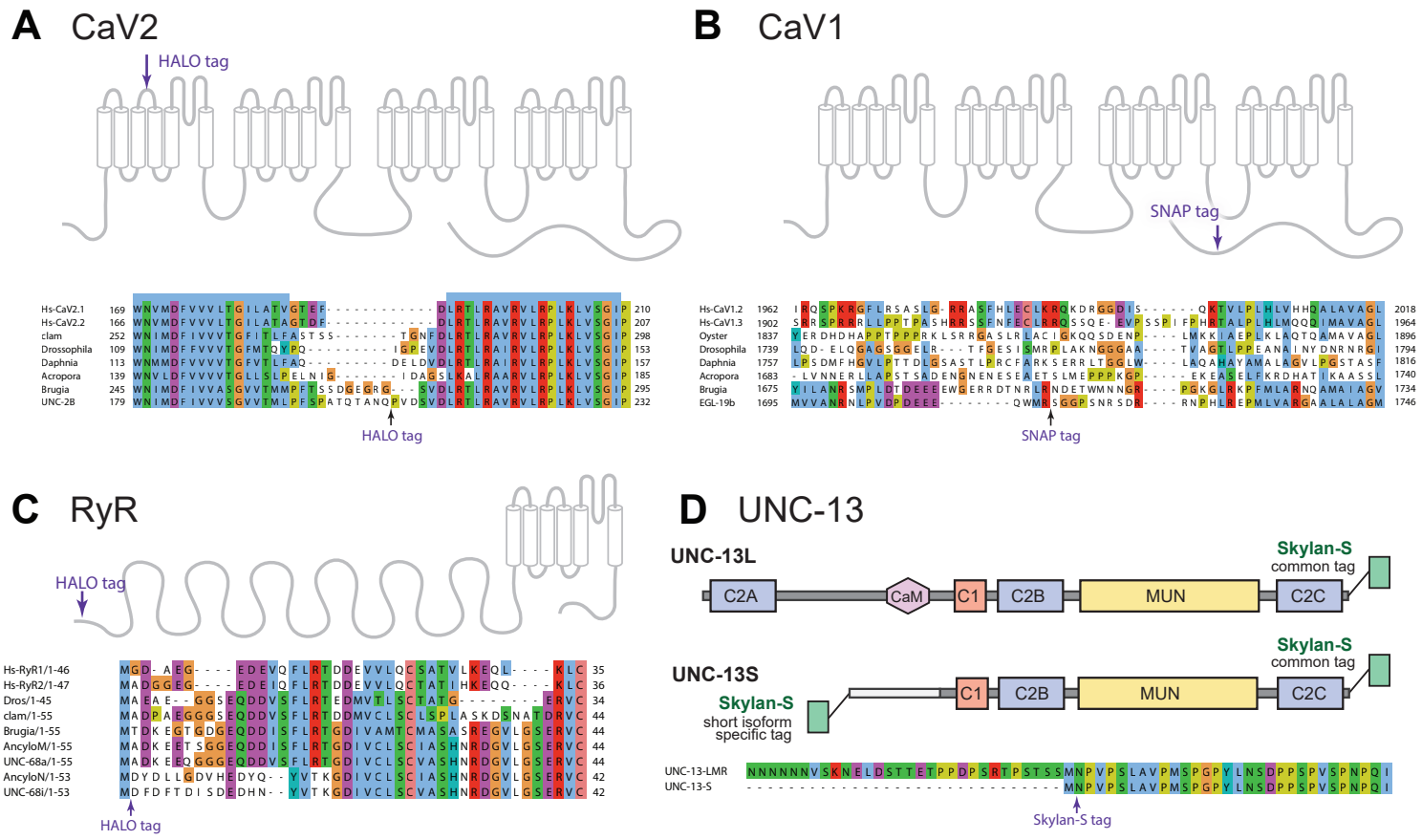
A CaV2
HALO tag
Hs-CaV2.1
Hs-CaV2.2
clam
Drossophila
Daphnia
Acropora
Brugia
UNC-2B
HALO tag
B CaV1
SNAP tag
Hs-CaV1.2
Hs-CaV1.3
Oyster
Drosophila
Daphnia
Acropora
Brugia
EGL-19b
SNAP tag
C RyR
HALO tag
Hs-RyR1/1-46
Hs-RyR2/1-47
Dros/1-45
clam/1-55
Brugia/1-55
AncyloM/1-55
UNC-68a/1-55
AncyloN/1-53
UNC-68i/1-53
HALO tag
D UNC-13
UNC-13L
Skylan-S
common tag
C2A
CaM
C1
C2B
MUN
C2C
UNC-13S
Skylan-S
short isoform
specific tag
UNC-13-LMR
UNC-13-S
Skylan-S tag

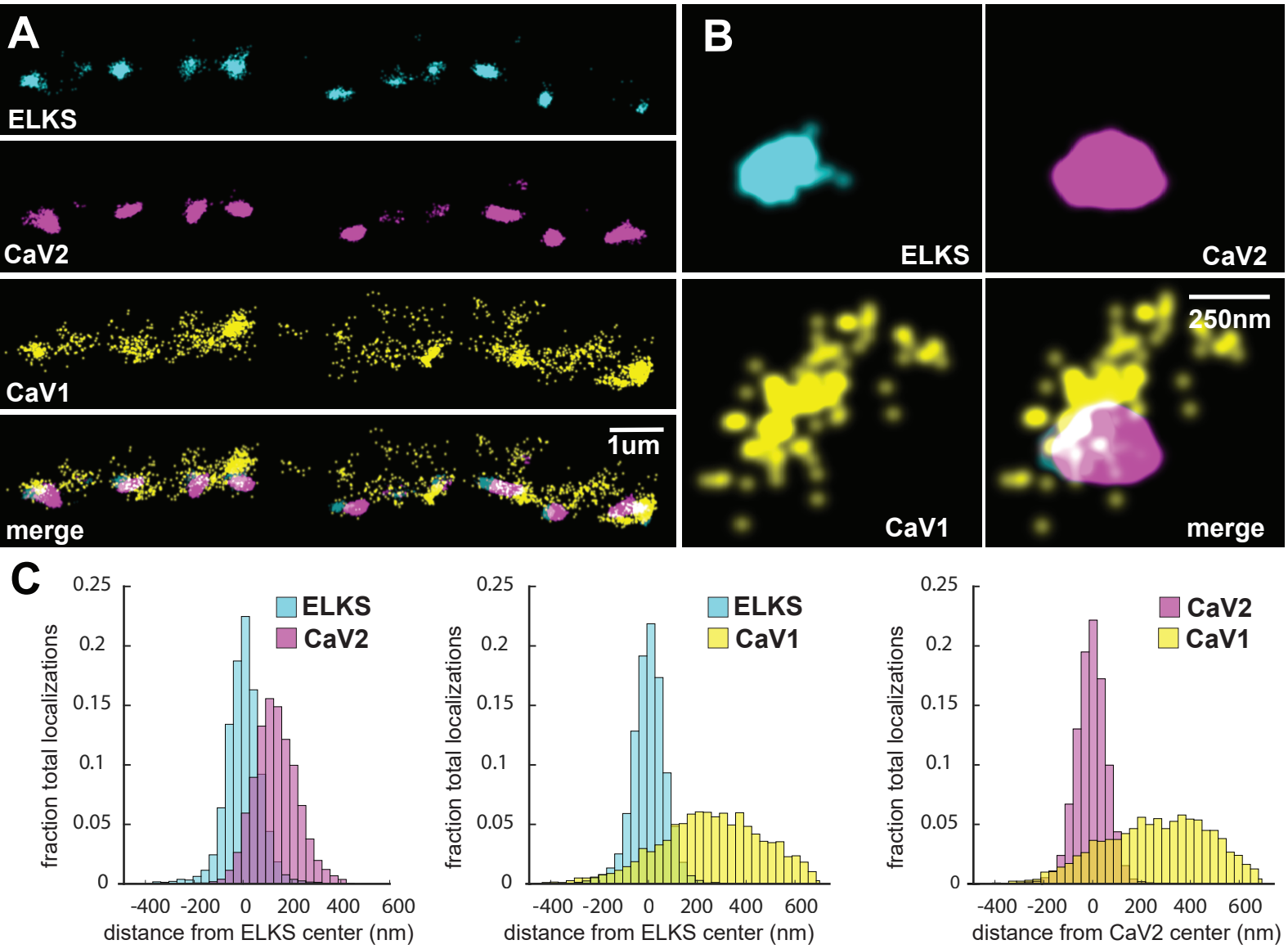
A
ELKS
CaV2
CaV1
1um
merge
B
ELKS
CaV2
250nm
CaV1
merge
C
ELKS
CaV2
fraction total localizations
distance from ELKS center (nm)
ELKS
CaV1
fraction total localizations
distance from ELKS center (nm)
CaV2
CaV1
fraction total localizations
distance from CaV2 center (nm)
0.25
0.2
0.15
0.1
0.05
0
-400 -200 0 200 400 600

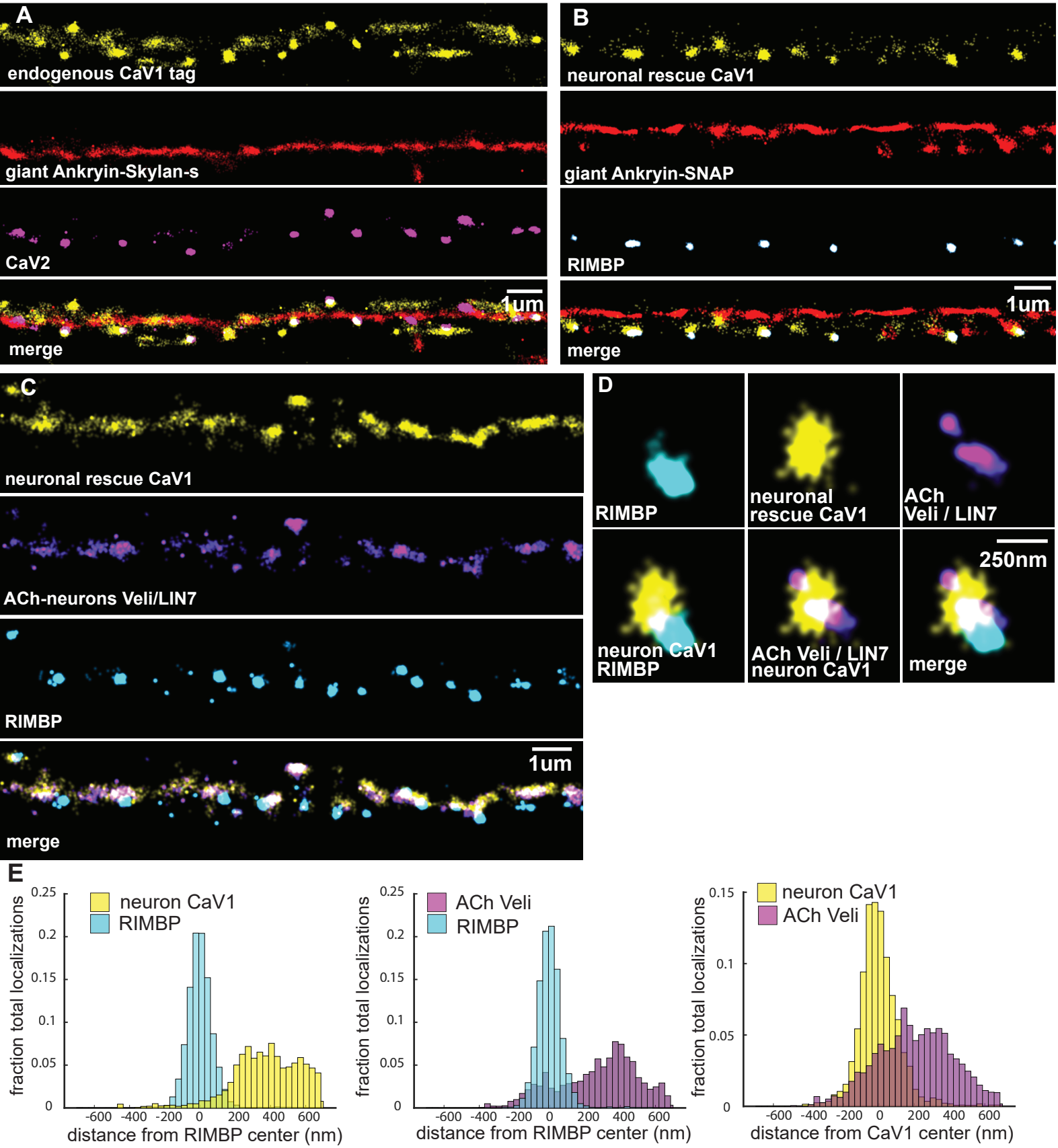
A
endogenous CaV1 tag
giant Ankryin-Skylan-s
CaV2
1um
merge
B
neuronal rescue CaV1
giant Ankryin-SNAP
RIMBP
1um
merge
C
neuronal rescue CaV1
ACh-neurons Veli/LIN7
RIMBP
1um
merge
D
RIMBP
neuronal rescue CaV1
ACh Veli / LIN7
neuron CaV1 RIMBP
ACh Veli / LIN7 neuron CaV1
250nm
merge
E
neuron CaV1
RIMBP
fraction total localizations
distance from RIMBP center (nm)
ACh Veli
RIMBP
fraction total localizations
distance from RIMBP center (nm)
neuron CaV1
ACh Veli
fraction total localizations
distance from CaV1 center (nm)

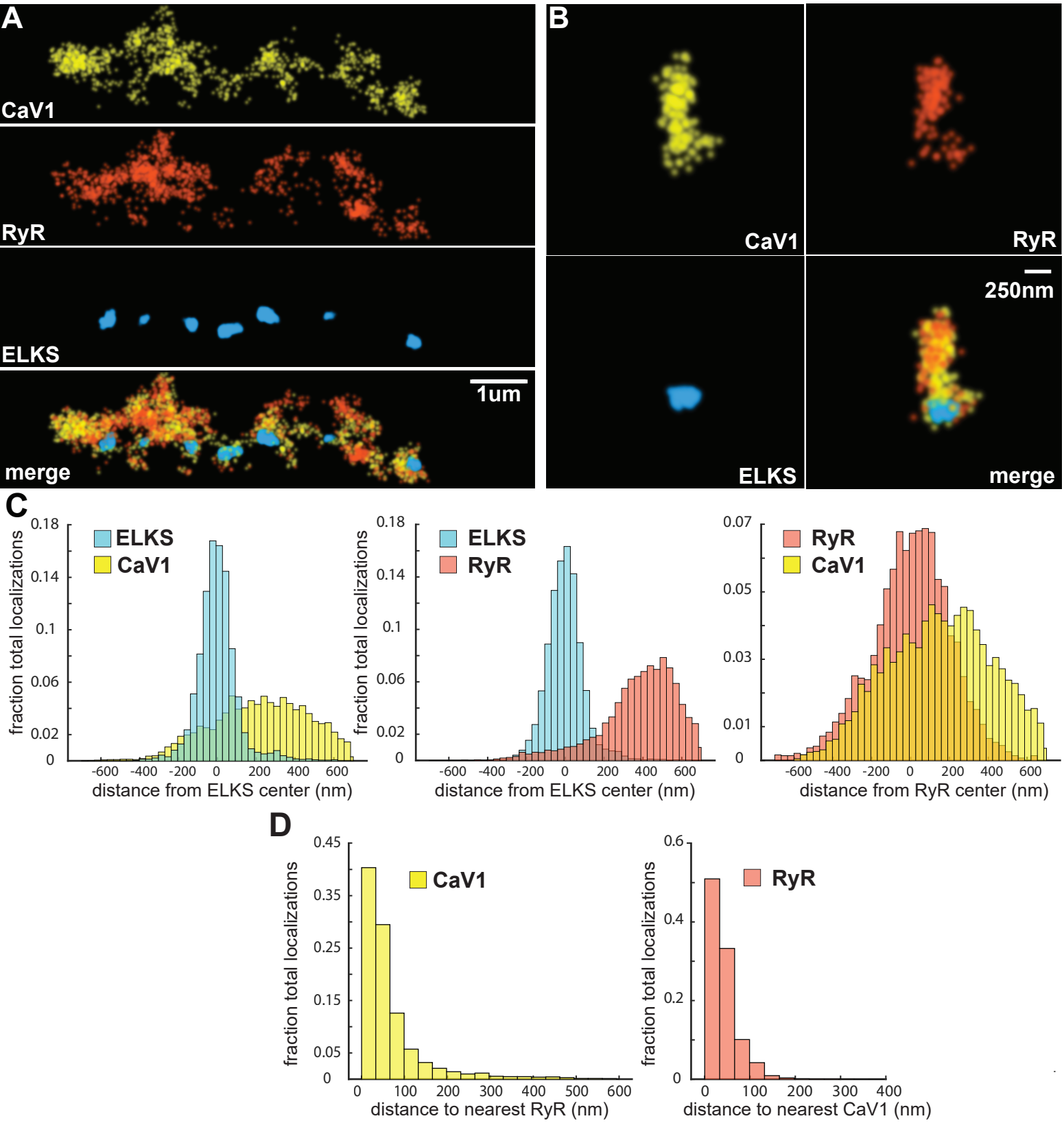
A
CaV1
RyR
ELKS
1um
merge
B
CaV1
RyR
250nm
ELKS
merge
C
ELKS
CaV1
fraction total localizations
distance from ELKS center (nm)
ELKS
RyR
fraction total localizations
distance from ELKS center (nm)
RyR
CaV1
distance from RyR center (nm)
D
CaV1
fraction total localizations
distance to nearest RyR (nm)
RyR
fraction total localizations
distance to nearest CaV1 (nm)

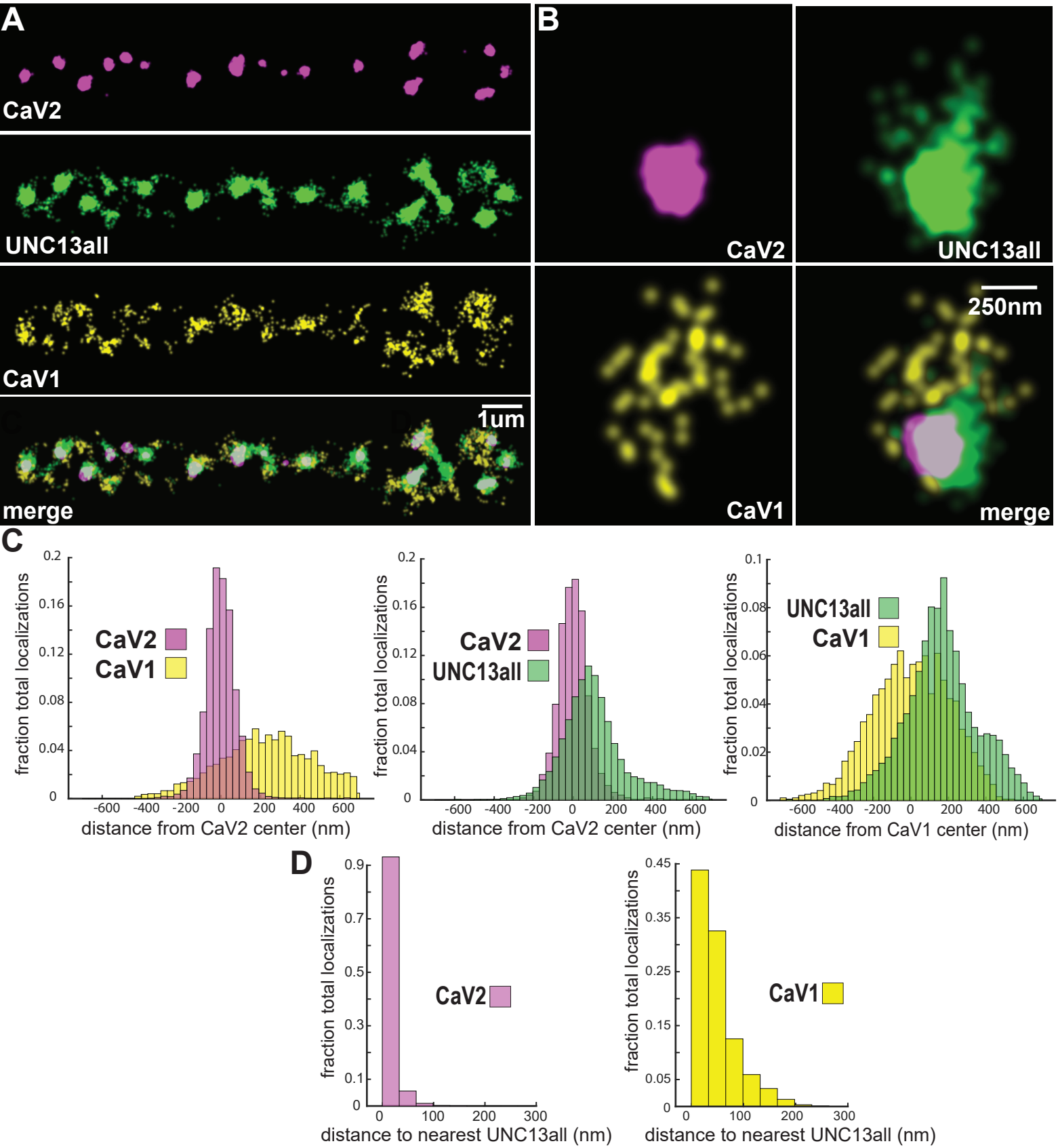
A
CaV2
UNC13all
CaV1
1um
merge
B
CaV2
UNC13all
CaV1
250nm
merge
C
fraction total localizations
CaV2
CaV1
distance from CaV2 center (nm)
CaV2
UNC13all
distance from CaV2 center (nm)
UNC13all
CaV1
distance from CaV1 center (nm)
D
CaV2
distance to nearest UNC13all (nm)
CaV1
distance to nearest UNC13all (nm)

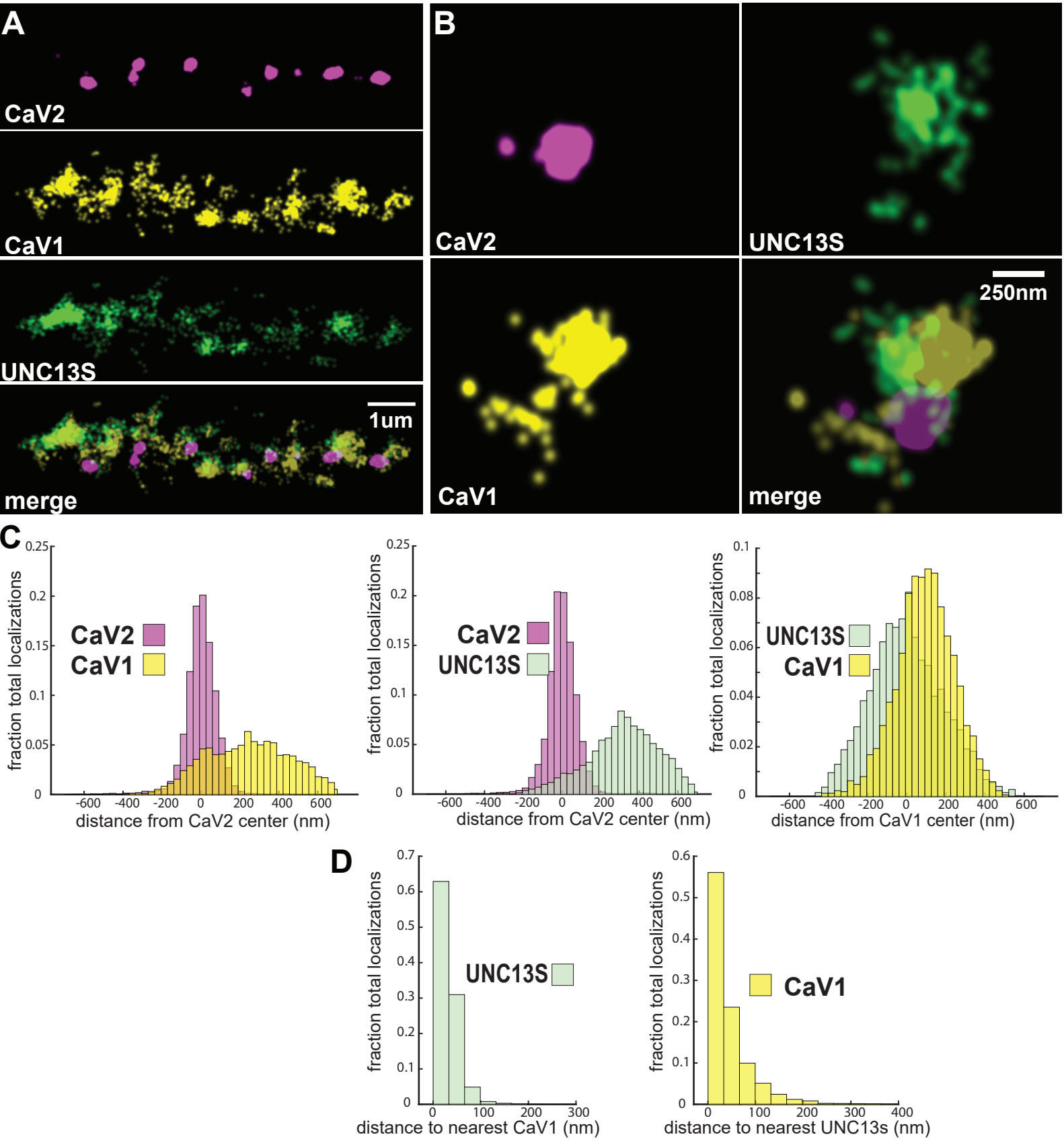
A
CaV2
CaV1
UNC13S
1um
merge
B
CaV2
UNC13S
250nm
CaV1
merge
C
fraction total localizations
CaV2
CaV1
distance from CaV2 center (nm)
CaV2
UNC13S
distance from CaV2 center (nm)
UNC13S
CaV1
distance from CaV1 center (nm)
D
UNC13S
distance to nearest CaV1 (nm)
CaV1
distance to nearest UNC13s (nm)

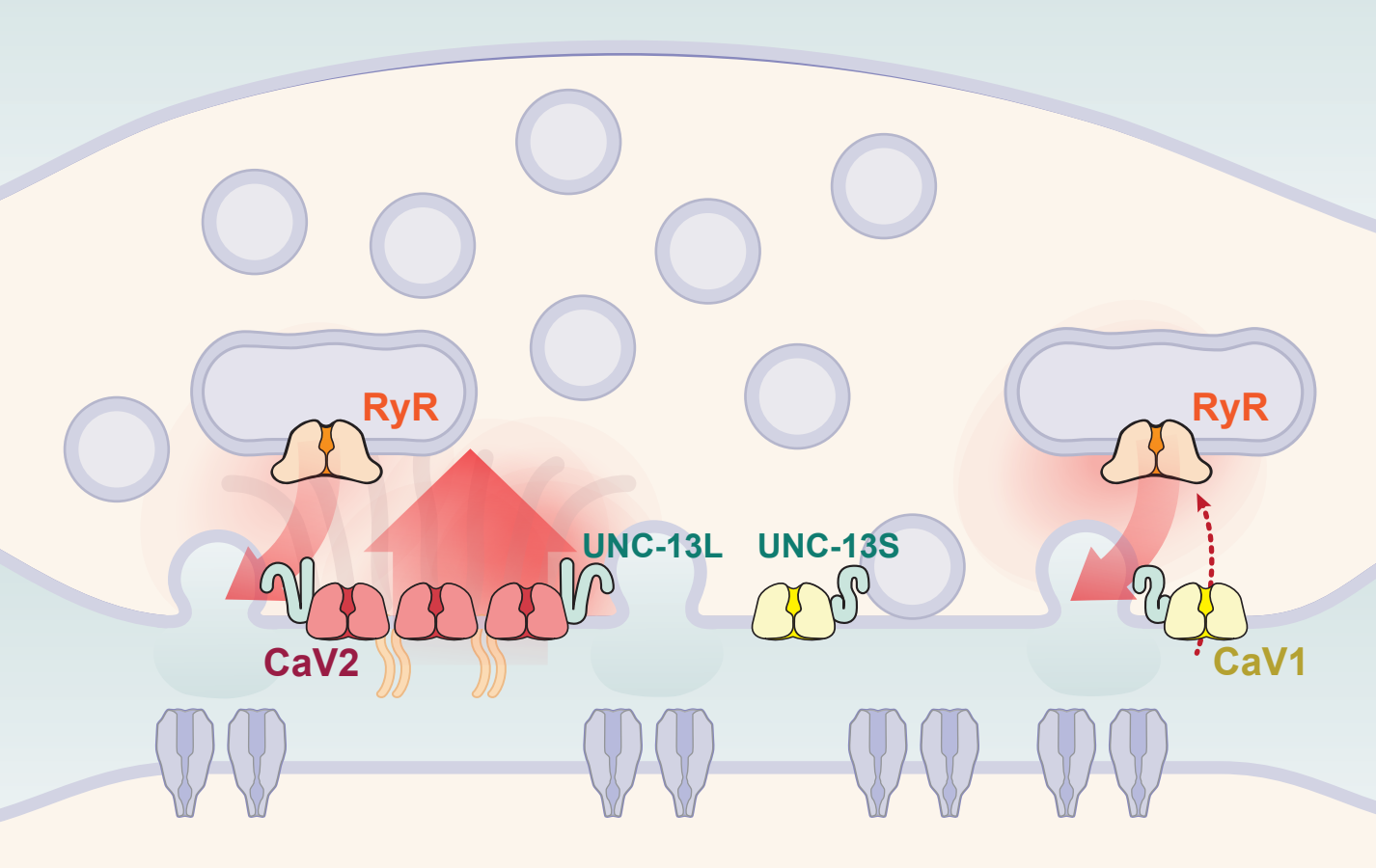
RyR
RyR
UNC-13L
UNC-13S
CaV2
CaV1